LLNL-JRNL-832174

Dynamics of Three-Dimensional Shock-Wave/Boundary-Layer Interactions

D. V. Gaitonde, M. C. Adler

February 28, 2022

Annual Review of Fluid Mechanics

ANNUAL REVIEWS

Annual Review of Fluid Mechanics

Dynamics of Three-Dimensional Shock-Wave/Boundary-Layer Interactions

Datta V. Gaitonde[1] and Michael C. Adler[2]

[1]Mechanical and Aerospace Engineering, The Ohio State University, Columbus, Ohio, USA;
email: gaitonde.3@osu.edu

[2]Weapons and Complex Integration, Lawrence Livermore National Laboratory, Livermore,
California, USA; email: adler5@llnl.gov

Annu. Rev. Fluid Mech. 2023. 55:291–321

First published as a Review in Advance on
October 19, 2022

The *Annual Review of Fluid Mechanics* is online at
fluid.annualreviews.org

https://doi.org/10.1146/annurev-fluid-120720-022542

Keywords

shock wave, boundary layer, turbulence, separation, three-dimensional, shear layer, stability, fluid/structure interaction, flow control

Abstract

Advances in measuring and understanding separated, nominally two-dimensional (2D) shock-wave/turbulent-boundary-layer interactions (STBLI) have triggered recent campaigns focused on three-dimensional (3D) STBLI, which display far greater configuration diversity. Nonetheless, unifying properties emerge for semi-infinite interactions, taking the form of conical asymptotic behavior where shock-generator specifics become insignificant. The contrast between 2D and 3D separation is substantial; the skewed vortical structure of 3D STBLI reflects the essentially 2D influence of the boundary layer on the 3D character of the swept shock. As with 2D STBLI, conical interactions engender prominent spectral content below that of the turbulent boundary layer. However, the uniform separation length scale, which is crucial to normalizing the lowest-frequency dynamics in 2D STBLI, is absent. Comparatively, the spectra of 3D STBLI are more representative of the mid-frequency, convective, shear-layer dynamics in 2D, while phenomena associated with 2D separation-shock breathing are muted. Asymptotic behavior breaks down in many regions important to 3D-STBLI dynamics, occurring in a configuration-dependent manner. Aspects of inceptive regions near shock generators and symmetry planes are reviewed. Focused efforts toward 3D modal and nonmodal analyses, moving-shock/boundary-layer interactions, fluid/structure interactions, and flow control are suggested as directions for future work.

1. INTRODUCTION

Shock-wave/boundary-layer interactions (SBLI) are a crucial determinant of the performance of high-speed vehicles. Typically, SBLI arise when the shock wave due to one surface, or a segment of it, interacts with the boundary layer developing on another. Regardless of whether SBLI occur in internal or external settings, the results are striking and usually disadvantageous from a vehicle-performance standpoint. Fluid-dynamic consequences include flow separation, vortical-structure formation, turbulence modulation, flow distortion, unsteadiness in various frequency bands, and localized amplification of heat transfer. Practical implications include loss of control-surface authority, increase in drag, reduction in combustion efficiency, and potentially destructive structural responses of panels and empennages.

As a consequence, SBLI have been the subject of extensive research over several decades. The state of the boundary layer entering the interaction is used to term SBLI as laminar, transitional, or turbulent. We focus mainly on shock-wave/turbulent-boundary-layer interactions (STBLI) in this review; however, results from the other regimes are noted in context when appropriate. The degree of flow separation varies with the interaction parameters, principally the Mach and Reynolds numbers, the strength and orientation of the shock relative to the boundary layer, and the wall temperature. We further restrict primary attention to strong interactions, in which the flow is separated in the time-mean sense; results for weakly (or incipiently) separated flows are noted when necessary to illustrate certain points.

Several comprehensive reviews mark key milestones in SBLI research. A suitable starting point for discussion here is the review of Dolling (2001), which has proven influential in providing focus for a large body of fundamental research efforts in the twenty-first century. Different aspects of SBLI, until approximately 2015, are summarized by Clemens & Narayanaswamy (2014), as well as Gaitonde (2015) and Sandham (2016). The goal of the current work is to spotlight recent work, that is, research since these later reviews that has contributed significantly to the current understanding of three-dimensional (3D) SBLI. For logical development and context, some prior efforts are also noted.

The preferred choices for fundamental SBLI studies are canonical arrangements that elicit the primary features of interest without overwhelming geometric complexity. A few examples used to illustrate the dynamics are shown in **Figure 1**. Results from such configurations have translated quite well to the practical setting involving high-speed vehicles; however, some scaling uncertainties remain. Statistically spanwise-homogeneous (or periodic) flows, especially the impinging-shock (**Figure 1*a***) and compression-corner (also known as compression-ramp; not shown in **Figure 1**) interactions, have been the most scrutinized. Both display similar dynamics insofar as the principal aspects are concerned, and it is generally accepted that they are equally applicable for studying the most fundamental properties of SBLI that are two dimensional (2D) in a time-averaged sense; of course, the instantaneous flow is 3D. Other 2D configurations that consider gradual curvature or sequences of compressions and expansions have also been explored, but not with as much vigor in recent years as the impinging-shock and compression-corner SBLI.

Recent multinational interest in high-speed flight is manifest in programs such as HIFiRE (United States–Australia), Sharp Edge Flight Experiment (Europe), Starry Sky-2 (China), and Hyper-Velocity Gliding Projectile (Japan). These vehicles engender SBLI in internal and

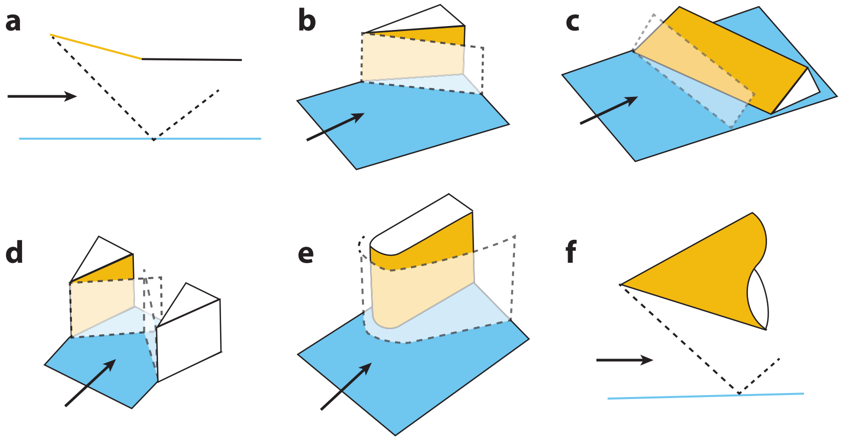

Figure 1

Canonical shock-wave/boundary-layer-interaction configurations of recent interest: (*a*) impinging shock, (*b*) sharp fin, (*c*) swept compression ramp, (*d*) double fin, (*e*) blunt fin or cylinder on plate, (*f*) cone above plate. The shock-generating surfaces are gold, the plate surfaces fostering the incoming boundary layers are blue, and the shocks are outlined with dashed lines. The direction of each incoming flow is indicated by an arrow.

external circumstances, in which no homogeneous direction is apparent; such 3D SBLI pose several additional challenges to their study relative to 2D SBLI, and the much larger number of possible orientations between the shock and the boundary layer requires the introduction of different abstractions to describe these interactions in a fundamental way. The examination of 3D SBLI also yields considerably more data that require greater sophistication in acquisition, visualization, and analysis.

Nonetheless, several canonical configurations have aided the exposition of the primary features; Settles & Dolling (1986) describe a comprehensive set, including classification into categories of semi-infinite versus protuberance and dimensional versus nondimensional. In this review, we consider the small subset illustrated in **Figure 1*b*–*f***, which include the sharp-fin (SF), swept-compression-ramp (SCR), double-fin (DF), blunt-fin (BF) or cylinder-on-plate (CoP), and cone-above-plate (CaP) configurations, because these have been the focus of some of the most intense, recent, fundamental research activity. Each configuration includes a surface (or plate) that fosters a 2D, turbulent boundary layer, which subsequently interacts with the shock due to a generator, yielding different 3D-SBLI phenomena.

The landmark review of Dolling (2001) summarizes the principal findings until the start of the twenty-first century. Notable features associated with the mean flow were fairly well established at the time for the 2D and many of the 3D configurations of **Figure 1**. A major contribution of the review by Dolling was to bring attention to the primary unknown SBLI issues: unsteadiness and heat-transfer rates. Progress has been made in both areas since then, especially for the former problem. SBLI display a wide range of amplified frequencies that may be delineated into distinct bands, with prominent spectral content well below that characteristic of the incoming boundary layer. Such low-frequency oscillations have the potential to trigger structural responses, including fatigue, and are thus of great concern.

Clemens & Narayanaswamy (2014) clarified community viewpoints regarding the origins of the low-frequency content. The context of upstream versus downstream influences has proven useful to the characterization, that is, to what degree the spectral facets of the interaction are necessarily dependent on fluctuations in the incoming boundary layer and/or the features of the separation bubble and downstream coupling. A related approach to understanding 2D SBLI considers the interaction in terms of a dynamical system that may exhibit features associated with amplifiers or oscillators. Although 3D SBLI are the primary focus of this work, the results concerning 2D SBLI form a reference for deliberation and are therefore summarized in Section 2. Since the publication of Clemens & Narayanaswamy (2014), a number of additional efforts on 2D SBLI, many leveraging tools from hydrodynamic stability and related viewpoints, have greatly added to the understanding of the community; we take the opportunity to outline some of these, because they too aid in the discussion of 3D SBLI.

With regard to the issue of heat-transfer rates raised by Dolling (2001), the primary concern is that these can be considerably amplified, by an order of magnitude or more, relative to those in the incoming boundary layer, but were difficult to predict or understand. Progress in understanding heat-transfer mechanisms since Gaitonde (2015) is not considered in this review; however, some issues are discussed in Section 4 regarding suggested future work.

The main focus of this review concerns the rich dynamics of 3D SBLI that have been elucidated by recent efforts. The differences in flow structure between these configurations and 2D SBLI are profound and include unique kinematic, topological, and dynamic features that are quite nonintuitive. For example, 3D separation is not necessarily accompanied by regions of reversed (to the freestream) flow and is generally achieved without zero skin-friction values (except at a few critical points). Similarly, 3D separating streamlines do not reattach, in contrast to 2D separation; this is even true on symmetry planes, such as those encountered in the DF, BF/CoP, and CaP configurations.

By the turn of the twenty-first century, classical efforts had established a number of databases (Settles & Dodson 1994) that characterized the flow past many of the configurations in **Figure 1**. Characterization of the mean flow relied mainly on qualitative surface-oil-flow and schlieren images, supplemented by quantitative, time-averaged pressure, skin-friction, and heat-transfer-rate measurements on the surface, along with field pitot-pressure surveys. Simulations were restricted mainly to Reynolds-averaged Navier–Stokes (RANS) approaches. Gaitonde (2015) surveys some of these 3D-SBLI results. In regions far removed from the shock generator, asymptotic dynamics are indicated by interaction properties that exhibit some degree of similarity (or symmetry) with respect to a suitably chosen reference frame; these properties provide an effective unifying schema to describe aspects of the interaction, such as 3D flow separation, and facilitate the derivation of scaling laws based on Mach and Reynolds numbers. Particular benefits of such descriptions include the simplifications associated with the classical free-interaction principle (Chapman et al. 1957), which delineates aspects of separated flows that are independent of the specific relative orientations of the shock and the boundary layer, as well as classifications into open-versus-closed separation and conical-versus-cylindrical symmetry. Pertinent results describing the mean flow are reviewed in Section 3.1 by assimilating new or revised observations into the classical mosaic.

The progress toward understanding unsteadiness in 2D interactions, which was documented by Clemens & Narayanaswamy (2014), triggered extensive subsequent corresponding studies of 3D interactions, with different relative orientations between the shock(s) and the boundary layer. In addition to the distinctions between 2D and 3D interactions noted above, the introduction of sweep yields variable crossflow shear layers and skewed separating shear layers in 3D SBLI, which engender new scales and phenomena that can append to or nullify 2D mechanisms. These efforts have applied considerably more advanced measurement and simulation techniques to expand the understanding of unsteadiness in 3D SBLI from the classical characterization, which had depended primarily on local, experimentally obtained, pressure measurements.

Recently developed, or maturated, high-resolution diagnostic capabilities for 3D SBLI include pressure-sensitive paints with superior spectral-response characteristics, high-speed schlieren, stereo particle image velocimetry (PIV), tomographic PIV, and even plenoptic cameras for volumetric measurements. Emphasis has also been placed on addressing the possible influence of tunnel-specific effects and scaling behavior through analogous campaigns in different facilities. Concurrently, the maturation of unprecedented simulation capabilities based on advanced algorithms and massive supercomputing resources has allowed for the resolution of all relevant spatiotemporal scales in turbulent, 3D SBLI, as well as the application of sophisticated dynamical systems approaches that can monitor enormous numbers of degrees of freedom. Both experiment and computation have also benefited from the concomitant development and application of data-driven postprocessing methods rooted in system-identification techniques. Collectively, these studies paint a complex picture of the underlying physics of unsteadiness in 3D interactions. These efforts and the conclusions that constitute the current understanding of the phenomenology and mechanisms of unsteadiness in asymptotic 3D SBLI are distilled in Section 3.2.

Although useful for connecting different types of 3D SBLI, the abstraction of asymptotic dynamics breaks down in many important circumstances. The details then become specific to the particular configuration of interest, and, in treating these special cases, restrictions must be placed on the scope of this review for tractability. Section 3.3 discusses some deviations relative to asymptotic behavior by focusing on regions of inception and symmetry. Inceptive effects refer to SBLI properties near the shock generator; practical configurations necessarily display such behavior in some neighborhoods, which may be quite large depending on the Reynolds number and strength of the interaction. Symmetry planes often bound regions of SBLI, and their apparent local similarity to the strictly 2D interaction has motivated the use of correspondences between the two; however, such correspondences must be interpreted with caution. Key distinctions between the dynamics associated with symmetry planes and 2D SBLI are elucidated, noting that deviations depend on the nature of the configuration; observations from the DF, BF/CoP, and CaP are merged in the discussion of this point.

Finally, some thoughts on emergent and future work regarding the dynamics of 3D SBLI are presented in Section 4. In addition to the natural next steps to further the understanding of asymptotic behavior, SBLI-related phenomena during large-scale, nonperiodic shock motion, as relevant to propulsion-flowpath components, are placed in the context of corner flows that are subjected to shock interactions (confinement). The improved understanding of 3D SBLI due to recent progress, including descriptions of turbulent coherent structures and spectral content, is then used to comment on potential, multidisciplinary advances in fluid/structure interactions (FSI) and control.

We have made several necessary choices in writing this review. Key points are elaborated using figures from the authors' own computational work. This election is made only for the sake of convenience. Citations crediting antecedent and contemporary works, from both experimental and other numerical campaigns, are included to the extent possible, with the following caveat: Given that the goal is to highlight SBLI dynamics rather than to provide a comprehensive citation database, some germane recent work has inevitably and regrettably been omitted from discussion and citation, due to the finite effort and perspective of the authors; such omissions should not be construed to impute irrelevance. To focus the discussion, we employ the SF configuration to describe the features of swept SBLI; similarities and differences relative to other configurations are summarized in reference to the SF flowfield. The results are assimilated from campaigns covering a wide range of Mach and Reynolds numbers. The former range spans approximately 2 to 5, while the latter, based on the incoming boundary-layer thickness (Re_δ), spans from $\mathcal{O}(10^5)$ in simulations to $\mathcal{O}(10^6)$ in experiments. While some 2D and 3D simulations match the Reynolds numbers of

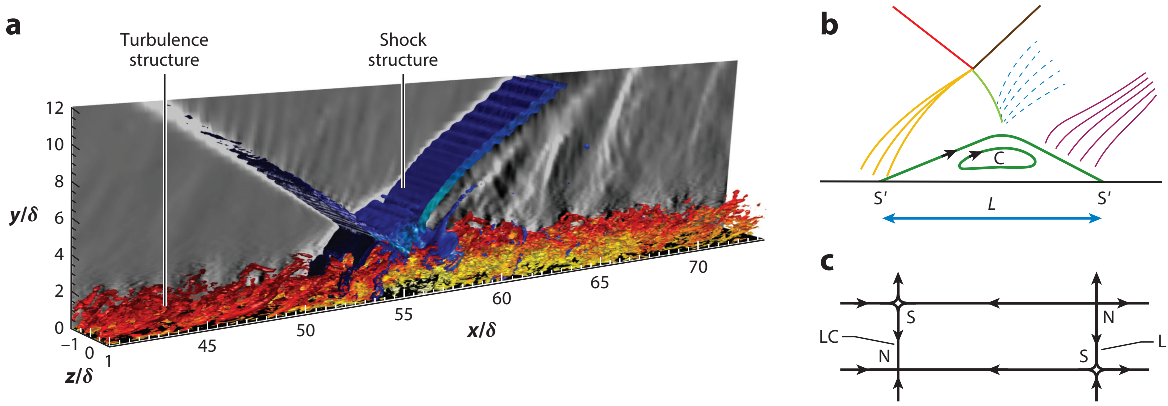

Figure 2

Flow structure of 2D shock-wave/boundary-layer interactions, as exemplified by the impinging-shock interaction. (*a*) Rendering of the instantaneous flowfield, with the turbulence structure described by the red colormap and the shock structure described by the blue colormap. Panel *a* adapted from Adler & Gaitonde (2018) with permission. (*b*) Illustration of the 2D mean flow, including the shock structure and streamlines in both the separated and the recirculating flow. (*c*) Sketch of the mean surface-flow pattern, illustrating the spanwise-degenerate surface-flow singular points: the spanwise-repeating, alternating nodes and saddles of separation and attachment that, in aggregate, form the LC and LD. Abbreviations: C, center; *L*, separation length; LC, line of coalescence; LD, line of divergence; N, node; S, saddle point; S′, surface saddle point.

experiments, many consider values an order of magnitude lower for computational tractability. The broad portrait of swept SBLI that is presented below is relatively independent of these parameters; therefore, specific parameters for different cases are listed explicitly only when necessary. Relatedly, details of the diagnostics and algorithms are also deferred to the cited literature.

2. 2D SBLI: SUMMARY AND UPDATE

The problem of establishing the causal description of unsteadiness has been a dominant driver of 2D-SBLI research since the review of Dolling (2001). Impinging-shock and compression-corner results are used interchangeably in this discussion because of their similarity for this purpose. **Figure 2*a*** shows some representative, instantaneous features of 2D SBLI. An equilibrium turbulent boundary layer (thickness δ) interacts with an impinging shock, resulting in flow separation. A schematic of the mean flowfield, shown in **Figure 2*b***, depicts the shock system, whose main components are the impinging and reflected shocks, which become separation and attachment shocks in the boundary layer, together with various compression and expansion waves.

The topological structure of mean-flow streamlines is relatively simple for this 2D interaction; however, it contains useful information as reference for the subsequent discussion of 3D SBLI. Zero-velocity points in the flow with indeterminate gradients, designated as critical (or singular) points (Perry & Chong 1987), aid in classifying and understanding the topological structure. For 2D separation, the primary singular points on the spanwise-normal plane are the center, C, and two saddle points (S′). The primes denote points occurring on the surface; rules governing the numbers and types of such points in surface-flow patterns or streamlines constrained to any arbitrary plane may be found in Perry & Chong (1987). More advanced bifurcations to both the surface and the off-surface flows may occur, including secondary separation and attachment; however, these are not crucial for the current discussion. This relatively simple, time-averaged structure is useful for analysis, but neither instantaneous streamlines nor pathlines in the turbulent flow follow such ideal, closed trajectories. The idealized, mean, surface-flow pattern, sketched

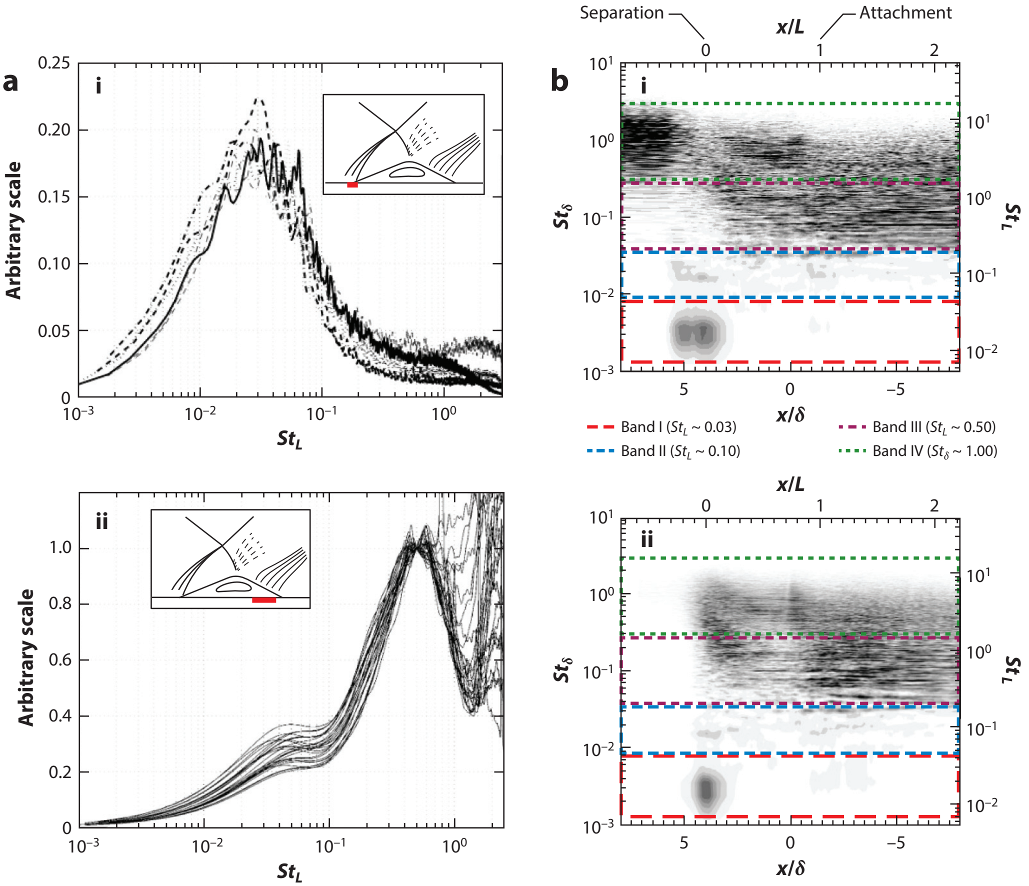

Figure 3

Characterization of unsteadiness in 2D shock-wave/boundary-layer interactions. (*a*) Premultiplied wall-pressure PSD at the shock foot (*i*) and near attachment (*ii*), for the impinging-shock interaction, with the Strouhal number formed from the mean separation length, St_L. Different lines in plots represent shock strengths varying from turn angles of 7.1° to 9°. The insets identify the regions of the interaction that exhibit the spectra of panels *i* and *ii*. Panel *a* is adapted with permission from Dupont et al. (2006) and is annotated for clarity. (*b*) Premultiplied wall-pressure PSD as a function of streamwise coordinate (x), with spatially local (*i*) and global (*ii*) normalization, for the compression-corner interaction; St is formed from the mean boundary-layer thickness (*left axis*) and the mean separation length (*right axis*). The colored bands call out important dynamics of the interaction: interaction breathing (*red*), secondary bubble oscillations (*blue*), shedding and shock flapping (*magenta*), and incoming turbulent fluctuations (*green*). Abbreviations: PSD, power spectral density; St, Strouhal number. Data from Adler & Gaitonde (2020) with permission.

in **Figure 2*c***, includes a line of coalescence (LC), where the flow separates from the surface, followed by a line of divergence (LD), where the flow reattaches; the distance between the two is the separation length (L). The comprehensive review of Green (1970) discusses the spanwise degeneracy of this 2D surface-flow pattern, which becomes nondegenerate, with important ramifications for unsteadiness in 3D SBLI.

The essential elements of unsteadiness in 2D SBLI, based on a large number of studies (Dolling 2001, Clemens & Narayanaswamy 2014), are illustrated in **Figure 3**. **Figure 3*a*** shows the premultiplied (by frequency) wall-pressure power spectral density (PSD) for impinging-shock interactions of different strengths ($7.1 < \theta < 9.5, \theta$ being the turn angle) at two locations. Near the foot of the separation shock, a peak is evident at $_L \equiv fL/U_\infty \sim 0.03$, in which St_L is the Strouhal number based on the frequency (f), the freestream velocity (U_∞), and L. L is clearly the relevant length scale to nondimensionalize the prominent low-frequency content that is found two decades lower than those frequencies representative of the incoming boundary layer. Downstream of separation, the peak frequency range is centered at higher frequencies around $St_L \sim 0.5$, still a decade lower than those frequencies characteristic of the incoming boundary layer. Experimental results on the compression corner may be found in Ganapathisubramani et al. (2007).

Numerous simulations, including those of Pirozzoli & Grasso (2006), Touber & Sandham (2009), Priebe & Martín (2012) and Morgan et al. (2013), have confirmed this behavior. Panel *b* of **Figure 3** shows numerical results for the 2D compression-corner interaction, taken from Adler & Gaitonde (2020) for easier assimilation of the 3D-STBLI results to follow. Here, the premultiplied wall-pressure PSD is described as a function of the streamwise coordinate (x), while the left and right vertical axes indicate Strouhal numbers in terms of δ ($St_\delta \equiv f\delta/U_\infty$) and L, respectively. The results exhibit a similar low-frequency ($St_L \sim 0.02$) peak near separation and a mid-frequency ($St_L \sim 0.5$) band downstream of attachment. **Figure 3*b*,*i*** utilizes a spatially local normalization for PSD, in which the frequency-integrated PSD at each spatial location is normalized to unity; this allows the prominent frequencies at different spatial locations to be compared independently of fluctuation magnitude. **Figure 3*b*,*ii*** utilizes a global normalization for PSD, which is useful for understanding which regions of the surface are subjected to significant dynamic loading, in this case, the regions near separation ($St_L \sim 0.02$) and attachment ($St_L \sim 0.5$).

A summary of 2D-SBLI phenomenology identifies four distinct bands marked in **Figure 3*b***, each with associated physical processes: band I ($St_L \sim 0.03$): interaction breathing and large-scale separation-shock motion, exhibited at the lowest frequencies and related to the properties and stability of the separated flow; band II ($St_L \sim 0.1$): secondary bubble oscillations, exhibited at the lower middle frequencies; band III ($St_L \sim 0.5$): large coherent fluctuations of the separated shear layer, including structure shedding and flapping of the reflected shock, exhibited at the middle frequencies (note that this band should be expected to scale properly only with a Strouhal number based on the properties of the shear layer); and band IV ($St_\delta \sim 1$): the convection and modulation of integral-scale turbulent fluctuations entering through the incoming boundary layer, exhibited at the highest frequencies.

Among these regimes, the most prominent range, which corresponds to the lowest band ($St_L \sim 0.03$), has been the subject of substantial additional attention since the review of Clemens & Narayanaswamy (2014), who address the interaction as a dynamical system, with driving mechanisms rooted in upstream boundary layer disturbances or in instabilities organic to the separation region. Their basic conclusion is that the latter mechanism is adequate to describe the observations, with the influence of upstream boundary-layer disturbances diminishing with the strength of the interaction, as represented by L.

Newer analyses have furthered our understanding of the low-frequency content in 2D SBLI. Flight-test data (Poggie et al. 2014) have revealed similarities with tunnel and numerical observations, laying to rest questions about whether tunnel or Reynolds-number effects (which tend to be much smaller in experiment and simulation than in flight) are responsible for these observations. Another noteworthy effort is that of Estruch-Samper & Chandola (2018), who use the flow past an axisymmetric step to delineate the role of the shear layer in the observed unsteadiness at different separation scales. Progress in perturbation-based analyses of time-invariant basic states, from both laminar and time-averaged turbulent flows, has also promoted deeper understanding. The rationale and justification for the latter to display dynamics representative of the fully turbulent flowfield, with Reynolds-stress considerations, have been developed anew (Beneddine et al. 2016, Karban et al. 2020), and successful applications of both modal and nonmodal techniques have been reported for a variety of problems in different speed regimes. Although all such exercises detect the tendency toward separation-bubble breathing, different insights have been obtained depending on the method, the basic state, and the interpretation. We focus on some efforts of the last few years to provide a basis for the 3D-SBLI results to follow.

Several studies have weighed in on low-frequency observations in the context of oscillator or amplifier dynamics. The laminar basic state, obtained at relatively lower Reynolds numbers, is steady; for these, stability analyses reveal only stable modes, requiring external forcing to sustain unsteady behavior. An example of a nonmodal analysis is presented by Sansica et al. (2014), who demonstrate that white-noise forcing of the bubble elicits a low-frequency response. Other methods using laminar basic states include the stability and global resolvent analyses of Guiho et al. (2016), who detect features of a selective noise amplifier and associate the lowest frequencies with structures near the separation shock. Of course, the impingement of a shock on a laminar boundary layer may trigger transition at typical parameters of interest; this problem is not in the scope of the current review, but Dwivedi et al. (2020) describe an example of the mechanisms involved at Mach 6.

For turbulent basic states, earlier efforts in this vein (Touber & Sandham 2009, Pirozzoli et al. 2010), which connected the low-frequency bubble-breathing phenomena to 2D global modes, were greatly extended by Nichols et al. (2017). An unstable zero-frequency mode was observed, which may be important to the oscillator characterization of the low-frequency dynamics, if the oscillator mechanism is fundamentally nonlinear (Adler & Gaitonde 2018, 2020). Nichols et al. (2017) additionally uncovered weakly damped modes consistent with bubble-oscillation behavior, presumably requiring external forcing for sustenance in the actual turbulent flow. There are a variety of possible sources for interaction forcing with both upstream and downstream origins. Upstream-traveling waves, observed and explained initially by Pirozzoli & Grasso (2006), were recently further connected to postseparated (downstream) flow influences on shock motion (Sasaki et al. 2021). Other simulations and correlations by Porter & Poggie (2019) draw attention to the influence of downstream-traveling boundary-layer fluctuations, originating upstream of the interaction, which may be influential in setting the phase of the low-frequency oscillations.

Recent high-fidelity simulations have also aided in connecting the observed low-frequency phenomena to unsteadiness in the underlying coherent structures. The mean streamline curvature of the separated SBLI flow allows for Görtler-like features (Andreopoulos & Muck 1987). Concerning a compression-corner flow, Priebe et al. (2016) highlight the influence of a Görtler-type instability and large-scale structures, which initiate at the shock foot and contain low- and high-momentum components that extend throughout the separation region. For strongly separated impinging-shock cases at high Reynolds numbers, Pasquariello et al. (2017) suggest that such coherent, Görtler-like vortices may provide a source of continuous forcing that is intrinsic to the interaction and influential in sustaining the low-frequency phenomena.

The dynamic linear response of the unsteady turbulent flow was recently examined using synchronized large-eddy simulation (Unnikrishnan & Gaitonde 2016), which considers statistical analyses of the initial-value problem and tracks linear perturbations propagating in the fully turbulent flow (Adler & Gaitonde 2018). This procedure introduces the concepts of time-local and time-mean linear tendencies and facilitates the examination of selective amplification at various points in the limit cycle of interaction-breathing motion and asymmetries and restoring mechanisms in the oscillatory cycle. The results confirm, clarify, and extend many of the observations derived from analyses of mean flows. In particular, the 2D SBLI exhibits a global absolute instability that is maintained through constructive self-sustaining feedback of perturbations in the separation region. The statistical analysis of perturbations in the low-frequency band identifies linear restoring tendencies at extreme shock displacements while indicating that the mean shock position is linearly unstable; hence, the oscillatory description of low-frequency motion must be fundamentally nonlinear. The time-mean linear tendency is for upstream shock motion, and the analysis assigns the asymmetry, as noted experimentally by Piponniau et al. (2009), as a consequence of competing linear and nonlinear mechanisms.

The mid-frequency band has not been scrutinized in as much detail as the low-frequency band. However, this spectral content is prominent in the interior of the interaction and in the separation (reflected) and attachment (impinging) shocks (**Figure 3*a***). The coherent structures associated with this band, assigned to shear-layer phenomena, are visualized, for example, in the experiments of Souverein et al. (2010). This band of frequencies has also been reproduced in high-fidelity turbulent simulations and stability studies. A major question from the standpoint of this review, being pertinent to 3D SBLI, concerns the appropriate length and velocity scales underlying the frequencies in this band; this discussion is deferred to Section 3.2.

3. 3D SBLI

3D-SBLI research in recent years has deployed ever-more-sophisticated computational and experimental techniques for the SF (Arora et al. 2019, Adler & Gaitonde 2020), SCR (Vanstone et al. 2018, Adler & Gaitonde 2020), BF/CoP (Lash et al. 2021, Lindörfer et al. 2020), CaP (Zuo et al. 2019), and swept impinging-shock (Padmanabhan et al. 2021) interactions. All of these have highlighted, to various extents, key distinctions between 3D SBLI and 2D SBLI, reinforcing the need to exercise care in interpreting results obtained for the former in the more mature frameworks developed for the latter.

Some simplicity and unity of description may be obtained by first considering the behavior of swept SBLI arising from semi-infinite interactions that give rise to an asymptotic state. Such flowfields are achieved at distances where the direct influence of the shock generator diminishes. We use the SF in Sections 3.1 and 3.2 to discuss the asymptotic features of 3D SBLI, drawing distinctions with the other configurations of **Figure 1** as necessary. Asymptotic and limiting dynamics are discussed in Section 3.3, using specific configurations for illustration.

3.1. Asymptotic Swept Interactions: Flow Structure

When one is describing the 3D nature of the flow, it is advantageous to examine the interaction from different perspective viewpoints. To provide orientation, the flow direction is marked as a common reference where appropriate. The SF SBLI of **Figure 4** illustrates both the instantaneous and the mean structure of a typical, swept, semi-infinite, 3D interaction. The rendering of the 3D interaction in **Figure 4*a*** is analogous to that of the 2D interaction of **Figure 2*a***. The incoming boundary layer is similar in both cases; however, the shock structure is distinctly different. Far above the plate, in the essentially inviscid region, the shock sweeps across the boundary layer at an oblique angle. Near the surface, the shock bifurcates to form a lambda (λ), with a leading segment, the separation shock, that induces flow separation and a trailing component, the rear shock. The shadowgraph of the flow in **Figure 4**, from Arora et al. (2019), displays a very similar instantaneous structure. The strength of the interaction, which controls the size of the lambda and the separated region, depends on the freestream Mach number and the flow turning angle (Korkegi 1975). 3D reconstructions of the flow from experiments, employing the tomographic PIV technique, also exhibit elements that are consistent with this 3D structure (Mears et al. 2021). Due to the similarity of swept, semi-infinite SBLI, analogous renderings of the SCR interaction display the same principal features (Adler & Gaitonde 2020).

The growth of interaction size with increasing distance from the leading edge of the shock generator draws attention to the type of behavior anticipated asymptotically, that is, far from the shock generator. The asymptotic behavior is best characterized with the mean flowfield, specifically, the

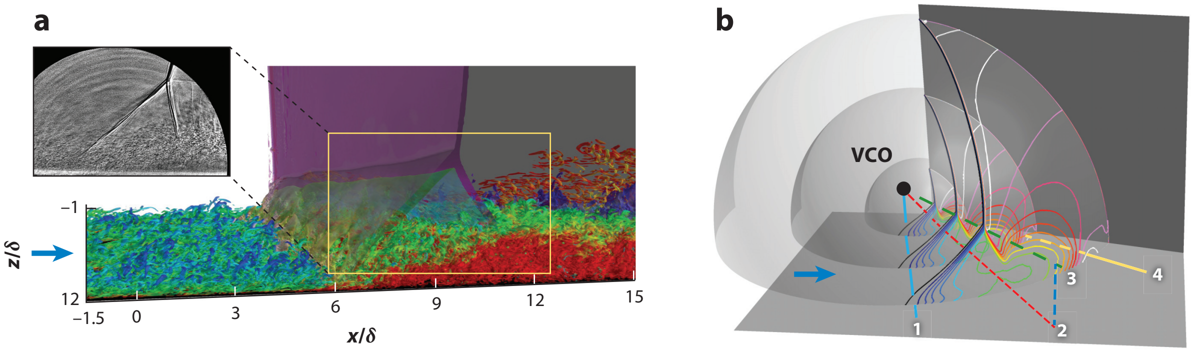

Figure 4

3D structure of the sharp-fin shock-wave/boundary-layer interaction. (*a*) An isosurface of Q-criterion colored by streamwise-velocity magnitude describes the instantaneous structure of the turbulence (*red/blue* colormap), with isosurfaces of $|\mathbf{u} \cdot \nabla p|$ to describe the instantaneous shock structure (*transparent blue/purple* colormap). The spatial coordinates are nondimensionalized by δ. The inset facilitates the comparison of the highlighted region to a shadowgraph image from the experiments of Arora et al. (2019), reproduced with permission. (*b*) Contours of the mean pressure on concentric, virtual conical origin (VCO)-centered, spherical surfaces illustrate the conical symmetry of the mean flow, with annotation of the fundamental lines of the interaction: (*1*) line of surface-flow coalescence, (*2*) projection to the plate of the inviscid shock, (*3*) shock-triple-point locus, and (*4*) line of surface-flow divergence.

type of symmetry ultimately attained. Two primary types of asymptotic symmetry, conical and cylindrical, arise in semi-infinite swept interactions with planar shock generators. In the former, a major focus of this review, the 3D mean properties collapse when plotted in spherical coordinates that originate at a point designated the virtual conical origin (VCO). This introduces a radial distance variable, r, originating from the VCO. **Figure 4*b*** illustrates the conical symmetry of the SF by plotting the mean pressure on concentric spherical surfaces centered at the VCO. The lambda-shock structure is evident on each spherical surface, growing in size linearly with r, and the locus through the shock triple points on each surface is essentially a straight line from the VCO, in the asymptotic limit.

The footprint of the flow, represented by experimental, surface-oil-flow patterns or bounded near-wall streamlines from simulation, also exhibits characteristics of conical behavior; such patterns are an especially useful description of the nature of the interaction because they can be obtained experimentally with a relatively more accessible measurement technique. **Figure 5*a*** shows a perspective sketch of the interaction footprint, including the fin. The surface flow of the incoming boundary layer forms an LC, indicating 3D separation; the LC is formed approximately at the foot of the separation shock, as shown in **Figure 4**. Nearer to the fin/plate juncture, an LD forms, indicating 3D attachment. The inviscid-shock trace lies between the LC and LD. These features are readily observable from both the experimental oil-flow patterns (Baldwin et al. 2019) and the simulated surface flow (Adler & Gaitonde 2019).

For interactions that exhibit conical symmetry in the asymptotic limit, the LC, the LD, and the shock-triple-point locus appear to originate from the VCO. Additional features, including those associated with secondary separation and attachment if present (Settles & Lu 1985), also appear to originate from the VCO in the asymptotic limit. Conical symmetry is increasingly imperfect and eventually broken in the inceptive region near the shock generator ($r \to 0$), where the surface-flow lines exhibit some curvature; the phenomena of this region are examined separately in Section 3.3. Therefore, the overall symmetry of the interaction, including inceptive effects, is termed quasi-conical. Notably, even far from the shock generator, the thickness of the boundary layer entering the interaction does not generally increase with r in the manner required for true

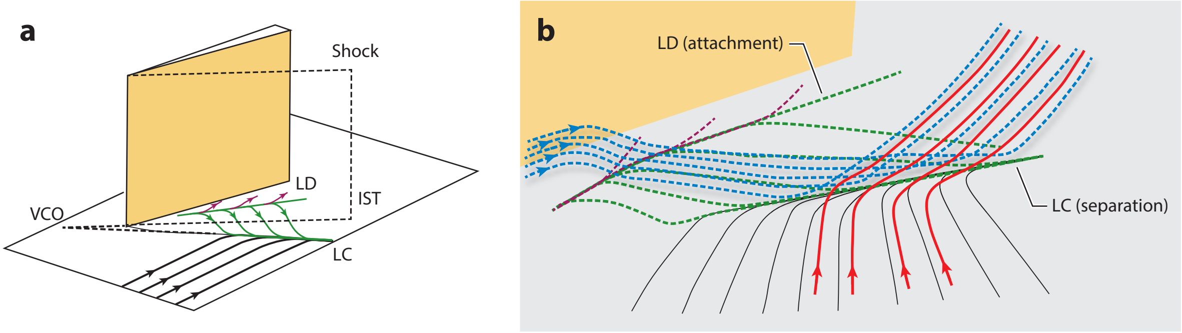

Figure 5

Separation structure of the 3D-SBLI mean flow as exemplified by the sharp-fin interaction. (*a*) Streamlines bounded to the near-wall region (*black*, *green*, *magenta*) illustrate the surface-flow LC (separation: *black/green*) and LD (attachment: *green/magenta*). (*b*) Bounded near-wall streamlines (*black*, *green*, *magenta*) along with unbounded streamlines (*red*, *blue*) illustrate the shear layer formed by the separating boundary layer (*red*), as well as the entrainment flow (*blue*). The attaching flow (*blue*: from above the plate surface on the *left*) has not previously separated; thus, it is not reattaching. Abbreviations: IST, inviscid-shock trace; LC, line of convergence; LD, line of divergence; VCO, virtual conical origin.

conical symmetry. However, because the interaction size itself increases with r, the thickness of the incoming boundary layer becomes insignificant relative to the size of the interaction, and conical symmetry becomes increasingly perfect ($r \to \infty$). The SCR interaction also exhibits quasi-conical symmetry; this quasi-similarity of the flow structure for 3D SBLI resulting from different types of planar shock generators forms a foundation for the free-interaction principle (Chapman et al. 1957).

The streamline structure of the 3D-SBLI mean flow is markedly different from that of its 2D counterpart. Representative streamlines are sketched in **Figure 5*b***. One may establish a connection between the unrestricted off-surface streamlines and the restricted surface-flow streamlines (the trajectories are restricted through their reprojection to the near-surface region). As in 2D SBLI, the LC in the surface-streamline pattern of the 3D SBLI indicates flow separation. However, unlike the former, after leaving the surface, the separating streamlines (**Figure 5*b***) of the latter yaw away from the shock generator, which is a manifestation of flow relief in this swept interaction; more crucially, these streamlines never reattach. Rather, the flow separating from the downstream side of the LC (**Figure 5*b***) is actually the same flow that attached at the line of divergence near the fin-plate junction. This fluid is swept toward the line of separation from the downstream side. Because this flow has already been processed by the swept shock at a higher elevation from the plate, the flow after attachment evolves under a favorable pressure gradient. The notion that separation and attachment regimes in 3D flows are profoundly different from each other and from corresponding processes in 2D flows has been noted numerous times over the years, even in the early reviews of Green (1970) and Délery (2001). The different origins of the separating and attaching flows in 3D SBLI, in the boundary layer and in the outer inviscid flow, respectively, lead to the notions of outer and inner regimes (Adler & Gaitonde 2019), with competing 2D and 3D scales that have no counterpart in 2D SBLI. In the context of the classical notion of such swept flows being inviscid/rotational outside of the region near the plate (Knight et al. 1987), one may then argue that the outer flow constitutes the vortical content arising from the upstream boundary layer, while the inner crossflow and far-outer rotational flow cause its redistribution.

The structure of the quasi-conical mean flow also provides insight into some important aspects that are tangentially related to this review. The observations of high pressure and heat-transfer rates near the juncture of the fin and the plate are related to the impingement of the outer flow (an impinging jet) in this region (Kim et al. 1991, Panaras 1996). The distribution of Reynolds stresses and turbulent kinetic energy have not been probed in quite as much detail as for 2D interactions; nonetheless, some understanding of these quantities may be found in Adler & Gaitonde (2019). Baldwin et al. (2021) explored the effect of scale by obtaining results in different facilities for interactions at similar Mach numbers but different Reynolds numbers; the results are similar in form, and a method of mapping between different interaction sizes has been proposed.

Although classical studies have confirmed the quasi-conical character of these swept interactions (Settles & Lu 1985, Gibson & Dolling 1992), a brief discussion of cylindrical symmetry is apt. In such interactions, flow similarity collapses in cylindrical coordinates. The lines of separation and attachment are parallel to each other, which is similar to the 2D case of **Figure 2*c***, except that a spanwise velocity component is superposed. Because the interaction footprint does not grow with the spanwise direction, the resulting dynamics necessarily differ from the results for conical symmetry discussed to this point. Classical literature suggests that the establishment of the type of asymptotic symmetry, conical versus cylindrical, may depend on whether the inviscid shock is attached or detached (Settles & Teng 1984). Recent high-fidelity simulations of SCR SBLI indicate that this is not the case (Adler & Gaitonde 2019); conical symmetry is always obtained in the asymptotic sense for swept, semi-infinite interactions. In cylindrical interactions, time-mean, aggregate entrainment of the outer flow is precluded, leading to a circumstance in which the mean interaction is closed and a separating streamline can reattach, similar to a 2D interaction. Additionally, a uniform separation length scale can be defined; however, unlike the 2D SBLI, any closed convective loop in the 3D mean flow is precluded by the nonzero spanwise velocity component.

In a limiting sense, cylindrical interactions represent the displacement of the VCO to infinity, which may be obtained in the limit of mild sweep in 3D interactions. The results of Padmanabhan et al. (2021), concerning a swept impinging-shock interaction, indicate cylindrical behavior in a region where the interaction may be considered quasi-infinite; increasing sweep displays an apparent tendency toward conical interactions. Vanstone et al. (2018) summarize their own prior observations to indicate that measurements of cylindrical symmetry in swept interactions may represent inceptive regions of otherwise conical interactions and, further, that truly cylindrical interactions may be limited to 2D SBLI.

Nonetheless, conceptually stimulating numerical exercises have leveraged the relative simplicity of cylindrical symmetry. Di Renzo et al. (2022), Gross et al. (2022), and Larsson et al. (2022) examine the addition of a spanwise velocity component, with spanwise-periodic boundary conditions, to an unswept 2D impinging-shock configuration. This two-dimensional/three-component (2D/3C) SBLI provides an intermediate condition between the 2D and 3D interactions, which may provide insight for the examination of the transition between regimes. These studies indicate that the size of the separation bubble increases relative to the purely 2D case and is composed of a shallow precursor separation bubble and an essentially triangular main component (Di Renzo et al. 2022, Larsson et al. 2022).

3.2. Asymptotic Swept Interactions: Characterization of Unsteadiness

The basic nature of unsteadiness in 2D SBLI may be discerned, as in **Figure 3**, by examining spectra of surface-pressure fluctuations at a relatively small number of locations. The growth of 3D SBLI with radius from the VCO considerably complicates the description of unsteadiness due to the larger volume of interest. Universal features of interaction symmetry in asymptotic regions may be exploited to simplify the characterization; the rest of this section addresses unsteadiness in conically asymptotic regions of the flow.

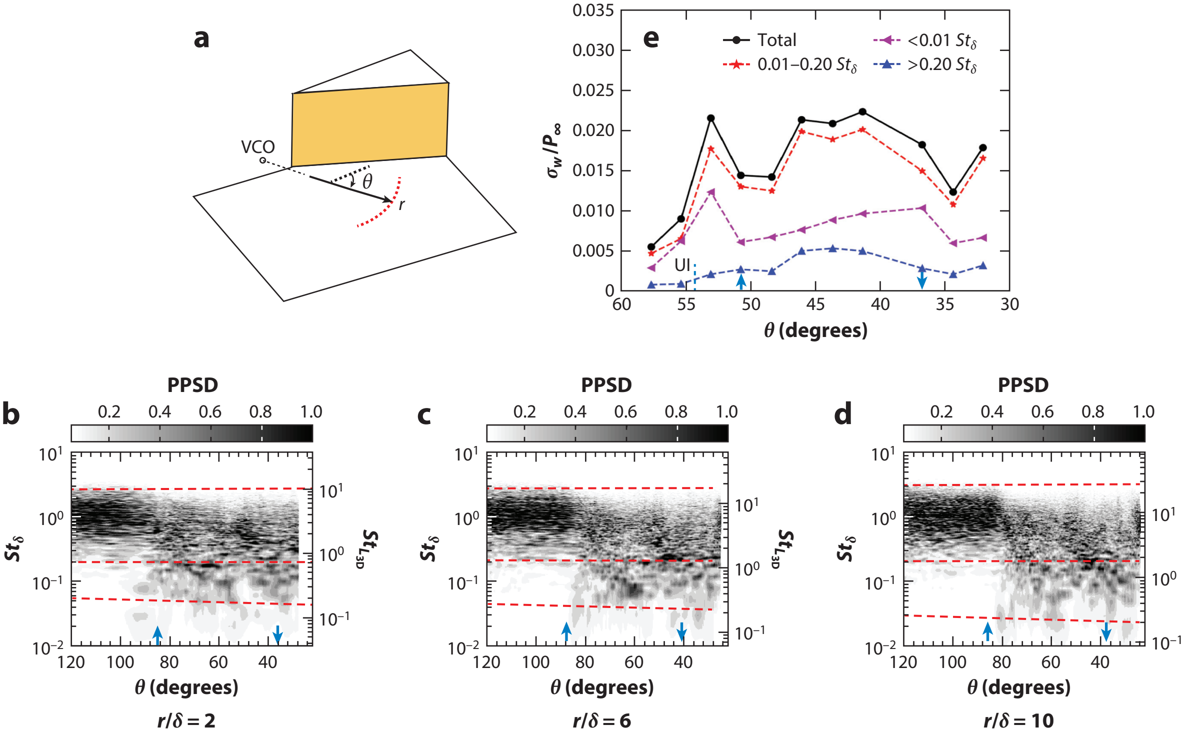

Figure 6

Characterization of unsteadiness in 3D shock-wave/boundary-layer interactions as exemplified by the sharp-fin interaction. (*a*) Schematic identifying the surface-pressure-probe locus (*red*) as a function of angle relative to the incoming flow direction (θ), at a given radius (r) from the virtual conical origin (VCO). (*b–d*) Premultiplied wall-pressure power spectral density (PPSD) as a function of θ at concentric radii: $r/\delta = 2$, 6, and 10 for panels *b*, *c*, and *d*, respectively. Frequency normalization is provided by Strouhal numbers (St) on the basis of the boundary-layer thickness (St_δ) on the left axis and local separation length $\left(St_{L_{3D}}\right)$ on the right axis. Bands demarcated by red lines outline the high-frequency (turbulence) and mid-frequency (shear-layer) bands. Blue arrows indicate lines of separation and attachment for the 22° interaction. Panels *b–d* adapted with permission from Adler & Gaitonde (2020). (*e*) Root-mean-square wall-pressure fluctuations as a function of θ for various frequency bands from the experiments of Arora et al. (2019) (adapted with permission) for the 15° interaction. The total spectrum (*black*) is shown along with constitutive components: middle frequencies (*red*), lower frequencies (*purple*), and higher frequencies (*blue*). UI denotes the upstream-influence line.

Because the properties of the interaction vary with the azimuthal angle (an angle of zero degrees corresponds to the freestream direction), it is convenient to plot the wall-pressure spectra along an arc at a specific radius from the VCO, as shown in **Figure 6*a***. We again use the simulations (Adler & Gaitonde 2020) to establish the main observations and then assimilate experimental data. Panels *b–d* of **Figure 6** show spectra for the SF interaction at three different radii for a 22° fin at Mach 2 and $Re_\delta \sim 1.6 \times 10^4$. The abscissa is the angle θ (**Figure 6*a***), with values in **Figure 6*b–e*** decreasing going rightward to maintain a left-to-right flow orientation, while the ordinate is the nondimensional frequency. Results from the simulated SCR are similar in form and may be found in Adler & Gaitonde (2020). Each arc intersects the LC and the LD, approximated as the locations of the leading and trailing shocks. The approximately vertical alignment of these locations indicates that the angle between them does not change with radial distance; that is, at these radii, the spatial distribution of the spectra exhibits conical symmetry. The distance (L_{3D}) along the arc between the LC and the LD clearly cannot be constant but increases with displacement, r, from the VCO; for this reason, the ordinate is marked in terms of both St_δ and $St_{L_{3\mathrm{D}}}$. The change in length, $L_{3\mathrm{D}}$, points to the growth of the interaction with r, and it serves as a local separation length scale but is not associated with a global, uniform, separation length as in 2D SBLI.

The simulated, asymptotic dynamics of these types of swept 3D interactions are distinctly different from those of 2D SBLI. This is evident from a comparison of the spectral bands of **Figure 6** with those of **Figure 3**; the quintessential comparison may be found in figure 5 of Adler & Gaitonde (2020). In particular, relative to the 2D SBLI, the swept SBLI exhibit a suppressed low-frequency band, that is, band I as designated in Section 2, with a peak at $St_L \sim 0.03$ that corresponds to $St_\delta \sim 0.006$ for these specific flow conditions. In fact, given St_δ, the most prominent band of low-frequency unsteadiness in these swept interactions lies only one decade below those frequencies characterizing the incoming boundary layer; without assigning equivalence at this point, this band was classified as mid-frequency (band III) in the context of 2D SBLI. In general, the spatial range of the mid-frequency band shows a measure of collapse in the conical frame. A vestige of a slightly lower frequency (that is, a frequency below the lower bound for shear-layer-associated unsteadiness in this interaction, as demarcated in **Figure 6*b*–*d***), occurring upstream of the location of the shock foot ($\theta \sim 90°$, $St_\delta \sim 0.03$), is evident only in the spectra at the smallest radius (**Figure 6*b***: $r/\delta = 2$). However, even this spectral content exhibits higher frequencies than those of band I of comparable 2D SBLI when scaled with the same δ. The integral-scale fluctuations scale with δ, while coherent shear-layer fluctuations scale weakly with the local separation length; this latter observation is clearer for the SCR, as noted by Adler & Gaitonde (2020). The more significant inceptive effects of the SF SBLI for small r in **Figure 6** cloud this latter observation; however, this interaction facilitates the subsequent illustration of the increasing influence of inceptive effects on the interaction dynamics as the VCO is approached ($r \to 0$).

The greater prominence of mid-frequency content in 3D SBLI relative to 2D SBLI has been reported preliminarily in the classical literature and comprehensively in the contemporary literature. In the former category are the SF studies of Gibson & Dolling (1992) and Schmisseur & Dolling (1994), as well as the SCR measurements of Erengil & Dolling (1993), all of which also describe the observed unsteadiness as being one order lower than the characteristic frequencies of the upstream boundary layer. Contemporary experiments by Arora et al. (2018) on a 15° SF SBLI at the same Mach number (2) but much higher Reynolds number ($Re_\delta \sim 1.5 \times 10^5$) than the simulations provide other key details. **Figure 6*e*** shows experimental results in the form of root-mean-square (RMS) wall-pressure fluctuations (σ_p) normalized by the mean wall pressure (P_w), for various frequency bands, obtained with Kulite transducers along a VCO-centered arc at a radius of approximately 13δ from the fin leading edge. The upstream-influence line and approximate separation and attachment locations are shown. **Figure 6*e*** shows the RMS of the full spectrum, along with that of three constitutive components separated by frequency range: low frequencies ($St_\delta < 0.01$), mid-frequencies ($0.01 < St_\delta < 0.2$), and high frequencies ($St_\delta > 0.2$).

The dominant component clearly lies in the mid-frequency range over most of the interaction downstream of the separation line. The RMS pressure is relatively high at the location of the shock foot, where both mid-frequencies and low frequencies show peaks. These experiments also provide some clarity regarding the motions of the separation and rear shocks, which result in variations of the size of the lambda structure with time; smaller lambda sizes are statistically more likely. The small, but coherent, increase in $St_\delta > 0.2$ content downstream of the separation shock is associated with the generation of smaller scales (near $\theta \sim 45°$) as the flow is processed by the unsteady separation shock. In terms of overall amplitudes, the measurements of Tan et al. (1987) indicate a general lowering of RMS pressure fluctuations in 3D interactions.

For the separated SCR at similar Mach and Reynolds numbers, Vanstone & Clemens (2019) divide the observed spectral content into slightly different Strouhal number ranges: $St_\delta < 0.01$, $0.01 < St_\delta < 0.1$, and $St_\delta > 0.1$, which they designate as low frequency, mid-frequency, and high frequency. This last range, despite its designation, contains portions of the band designated mid-frequency in **Figure 6**. Focusing on the separation line, they note that all bands contribute equally to the motion. However, the $0.01 < St_\delta < 0.1$ band correlates well with superstructures in the incoming boundary layer, with velocity structures being important in establishing the motion of separation location. In contrast, the $St_\delta > 0.1$ band does not correlate significantly with velocity fluctuations in the incoming boundary layer and accounts for large-scale unsteadiness in the interaction region. Rather, these frequencies are dependent on crossflow velocities, which increase with the degree of sweep and the size of separation structures. An intriguing observation (Vanstone et al. 2019) is that the spectral content of the shock foot motion differs from that of the separation line in that the former contains lower frequencies. In this context, the discussion of inceptive effects in Vanstone et al. (2018) becomes important (Section 3.3). The swept impinging SBLI results of Doehrmann et al. (2018), although cylindrically symmetric in nature, display some common behaviors of asymptotic conical interactions, including the rippling behavior of the shock front and increases of shock foot motion frequency with sweep.

Several aspects deserve scrutiny in associating the distinctions between 2D and 3D SBLI, regarding both the mean flow and the corresponding unsteadiness. The first concerns the separation length scale, L, as opposed to δ, that collapses the low-frequency band I data at different Mach and Reynolds numbers for 2D SBLI. For the conical symmetry exhibited by 3D SBLI, the separation and attachment lines are divergent, and no global length scale, which may be equally applicable at various distances from the VCO, is apparent. Therefore, scaling arguments from 2D SBLI do not seamlessly extend to conically symmetric 3D SBLI. One may then consider δ and the growth of interaction size with r to be, separately, imposing 2D and 3D scaling effects, respectively; these considerations provide a priori clues as to the observed differences in spectral content. Additionally, the lack of a clear correspondence between 2D and 3D scales indicates that similar values of Strouhal number, even when based on the same scale (for example, St_δ), do not permit an immediate association.

The second aspect concerns particle paths. As implied above, streamlines (or pathlines) in the unsteady turbulent flow do not loop upon themselves, regardless of whether the flow is nominally 2D or 3D. The time-mean flowfield is quite different and represents a useful abstraction to distinguish 2D from 3D flows. In the former, a convective streamline loop is obtained, while in the latter, regardless of the type of symmetry, whether conical or 3D cylindrical, the closed pattern is disrupted by the out-of-plane mean velocity component. This absence of a closed loop is also noted when such streamlines are restricted to arbitrary surfaces, such as spherical or spanwise-normal planes. In fact, as elaborated in Section 3.3, even on symmetry planes of 3D flows, the time-averaged flow exhibits a different streamline and critical point structure than those observed in **Figure 2*b***.

The third consideration concerns the natures of the two regimes displayed in **Figure 5*b***, the separating shear layer and the entrainment flow, which differ substantially from any 2D counterparts. The contours of **Figure 7** describe the local angles of pitch [**Figure 7*a***: $\arctan(v/u)$] and yaw [**Figure 7*b***: $\arctan(w/u)$] of the velocity vector, with streamwise, plate-normal, and spanwise components denoted by u, v, and w, respectively. The LC and the inviscid-shock trace are marked. The pitch angle exhibits both positive (near-separation) and negative (near-attachment) values. The yaw angle is uniformly positive, however, and takes values far exceeding the range plotted near the plate. A key observation is that the separating shear layer, which intersects the spherical surface at approximately the same location as the forward leg of the lambda shock,

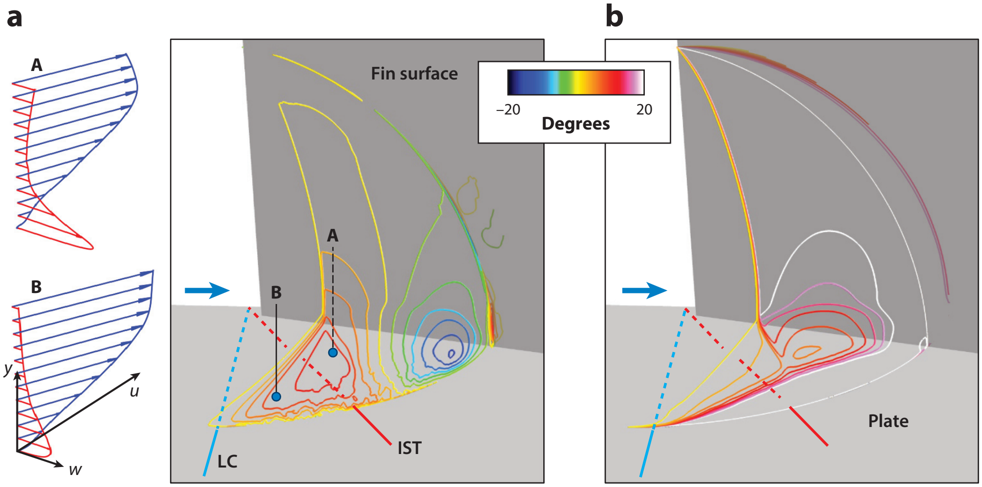

Figure 7

Aspects of the mean flow that highlight the separated shear layer and the entrainment flow. Contours of the pitch (*a*) and yaw (*b*) angles (in degrees) of the velocity vector are plotted on virtual conical origin–centered spherical surfaces of radius $r = 14$. Profiles quantify the mean streamwise (u) and spanwise (w) velocity components at locations downstream (A) and upstream (B) of the IST. Abbreviations: IST, inviscid-shock trace; LC, line of coalescence.

displays rapid spatial gradients of both pitch and yaw. This is indicative of its highly skewed, 3D nature, an initial impression of which is provided in **Figure 5*b***. Furthermore, the postattachment flow displays substantial crossflow velocities, taking the form of a skewed, wall-jet-like feature. Representative velocity profiles are displayed at two locations; the downstream profile is taken from a region where the outer flow is behind the inviscid shock, and the upstream profile is taken ahead of the shock. These profiles contain generalized inflection points; the compressible resolvent technique (Bae et al. 2020), assuming no streamwise or spanwise gradients, displays peaks at frequencies an order of magnitude below those of the incoming boundary layer. The potential clearly exists for excitation of additional mechanisms of instability; in this case, both traveling and stationary crossflow waves (Saric et al. 2003) may be supported. Given the known relationships between the unsteadiness observed in the flow and the stability properties of the mean flow, summarized above for 2D SBLI, the data suggest the possible presence of mechanisms that may also have no direct counterpart in 2D SBLI.

As noted above, corresponding nondimensionalized frequencies between 2D and 3D SBLI do not, by themselves, allow for conclusions regarding whether some elements of the 2D-SBLI mechanisms described in Section 2 are suppressed, left unaltered, or replaced by entirely new mechanisms in 3D; rather, the spectral content, which may manifest at different scales, must be connected to the underlying physical processes. Concerning the prominent postseparation band in 3D SBLI, Vanstone & Clemens (2019) indicate that frequencies in this band may be associated with coherent structures in the separated region that form alternating high- and low-velocity pairs. Their proper orthogonal decomposition modes from PIV data, designated as Group C and corresponding to frequencies $0.15 < St_\delta < 0.21$, indicate the presence of pseudostructures, or modal features or reconstructions similar to those in the observed velocity field. These are shed into the separation region and cause ripples in the separation line, traveling with the crossflow.

These characteristics are also prominent in the mid-frequency band of the simulations. Band-pass filtering analyses of the SF and SCR simulations along the plate as well as fin-parallel (SF) or spanwise-normal (SCR) surfaces are presented in Adler & Gaitonde (2020); these provide additional insights into the nature of the structures associated with these frequencies. Spatiotemporally coherent fluctuations are noted to travel with the outer (streamwise) and inner (crossflow) components of the postseparation shear layers. Being convective, these fluctuations bear some resemblance to the shedding frequencies ($St_L \sim 0.5$) associated with the postseparation shear layer of 2D SBLI (Agostini et al. 2012, Aubard et al. 2013). However, a crucial distinction is that the 3D shear layer is skewed in that it is formed by the two different regimes, as in **Figure 5*b***, and displays strong wall-normal gradients in the spanwise velocity component, as in **Figure 7**. The constructive and destructive interactions of pressure fluctuations in the mid-frequency band, resulting from the two obliquely aligned convection components of the inner and outer shear layers, result in periodic behavior, in which the primarily convective pressure fluctuations alternate between in-phase and antiphase switching, not unlike the observations of Vanstone & Clemens (2019).

The fully 3D, dynamical systems approach, originally developed for 2D SBLI by Adler & Gaitonde (2018), was repeated by Adler & Gaitonde (2020) for the 3D SCR using random, impulse forcing of the full state vector, at a location in the upstream boundary layer. In the context of the traditional theoretical framework and nomenclature as described by Schmid & Henningson (2012), the approach examines the spatiotemporal characteristics of nonmodal, linear perturbations associated with the maximum gain of the dynamical system due to a specific forcing impulse occurring at a specific instance of the turbulent flow. The generalized response characteristics may then be derived from the ensemble of specific statistical responses. In this formulation, for 2D SBLI, the nonmodal, linear perturbations associated with the maximum gain are self sustaining and remain confined to the separation region, indicative of an absolute instability, whereas for the swept 3D SBLI, the perturbations associated with the maximum gain are convective in nature, indicative of the absence of an absolute instability in the presence of convective instabilities. Moving from 2D to 3D SBLI, the correlation of this observation with the change in the SBLI dynamics related to the low-frequency mechanism in 2D interactions suggests that the instability necessary for enabling the prominent breathing motion of the shock wave in 2D SBLI is absent (or at least not significant relative to convective growth mechanisms) in strongly swept, 3D SBLI.

The effect of interaction strength has also been systematically examined by Adler & Gaitonde (2020). Stronger interactions result in larger coherent structures associated with the mid-frequencies; this is related to the nature of the 3D, separating shear layer, which becomes thicker and can support larger wavelength instabilities. A representative convective speed of these structures in the main separated region is $0.3U_\infty$, which is quite similar to those speeds in 2D SBLI (Aubard et al. 2013), and is generally independent of the 3D-interaction strength over the range explored. Aspects of the near-wall crossflow region, including the speed of convective structures, however, do depend on interaction strength; stronger interactions are less coherent and affected more significantly by the outer structures.

In conically symmetric regions, 3D autocorrelation peaks of fluctuations in the mid-frequency band increase in amplitude and period, which is consistent with the reduction of frequency and increase in coherence with increasing radial distance from the VCO. Because the flow velocity is similar at different radial distances, these observations are related to the radially increasing size and coherence of convecting coherent structures within the shear layers, which are associated with the mid-frequency band. Integral-scale turbulence in high-frequency bands exhibits amplification across the separation and attachment shocks, consistent with the shock/turbulence-interaction literature (Andreopoulos et al. 2000). High-frequency coherence is relatively low compared to the mid-frequency content, and it is also not very sensitive to the interaction strength or radial coordinate. The results suggest that, while the mid-scale coherent dynamics originate in the interaction as a result of instabilities of the skewed, postseparation shear layers, with mixed 2D and 3D scales, the higher-frequency content represents the amplification of components from turbulence in the upstream boundary layer, which imposes 2D similarity.

The observation that the primary mid-frequency unsteadiness in conical 3D SBLI is convective in nature and potentially related to instabilities of the postseparation shear layers naturally leads to the question of whether it may display properties that are only weakly dependent on the near-wall flow. Of particular interest are the scaling behavior and other properties that dictate the dynamics of this frequency band; is there a length scale that facilitates normalization of this content throughout the 3D interaction that is somewhat analogous to the separation length (L) in describing the similarity of low-frequency unsteadiness in 2D SBLI? The existence of such a length scale would simplify the analysis of 3D SBLI. Some clues may be obtained from the 2D-SBLI literature regarding the mid-frequency component (band III) associated with shear-layer phenomena, which has not been subject to the same level of scrutiny as the low-frequency band. The mid-frequency band is detected in stability analyses of laminar and turbulent-mean basic states. For example, Guiho et al. (2016) connect the scaling for mid-frequencies in a laminar, 2D, separated basic state to a measure of the boundary-layer displacement thickness. The shear layer in 2D SBLI occurs in a complex environment that includes the surrounding turbulent boundary layer, the instabilities resulting from low-frequency forcing, and the reversed flow on the lower side. Furthermore, entrainment preferentially occurs from the outer flow due to proximity to the wall on one side.

Nonetheless, recent experiments and high-fidelity simulations suggest that the properties of classical, free shear layers are recovered, even in this distinctly different local environment, where it is not obvious that near-wall effects would be negligible. Dupont et al. (2019) revisit the properties of the shear layers in 2D SBLI, choosing to examine stronger interactions, in which the scales of the mixing layer are more easily separated from the near-wall turbulence. For SBLI of two different strengths at Mach 2.3, they find, despite the proximity of the shear layer to the wall, that the shear layer exhibits similar turbulent shear stresses, spreading rates (if the peculiarities of the counterflow are properly accounted for), and entrainment velocities as in classical, free shear layers. In addition to validating earlier approximations (Piponniau et al. 2009), observations on anisotropy due to the vertical normal stress were leveraged to adapt the classical, dimensional considerations of Brown & Roshko (1974).

In fact, these commonalities with free shear layers apply over a wide parameter range. Helm et al. (2021) examine flows from Mach 2.9 to 9.1 with convective Mach numbers between 1 and 2. They confirm the applicability of classical considerations of flow similarity as well as other aspects, such as the development of rollers and subsequent breakdown to three-dimensionality, the reduction in spreading rate, and the anisotropy of the flow. This successful contextualization of complex, 2D-SBLI features in canonical constructs leads to the intriguing possibility that insights into the convective mid-frequency content of 3D SBLI may be similarly extracted by considering skewed 3D shear layers that are isolated from the more complex near-wall flow.

3.3. Nonasymptotic Regions: Inceptive and Symmetry-Plane Effects

Although conical symmetry provides a unifying framework for the asymptotic behavior of swept semi-infinite SBLI, it does not manifest in all regions of these interactions. In yet other configurations, including the BF/CoP and CaP of **Figure 1**, the primary shock weakens with spanwise displacement from the centerline, and the behavior at large distances from the shock generator becomes trivial. Such cases must necessarily be treated on a case-by-case basis because geometry-dependent scales and orientations become important.

To maintain focus relevant to conical symmetry, we consider two related contexts: inceptive regions near shock generators and symmetry planes. Several effects disrupt the flow pattern near

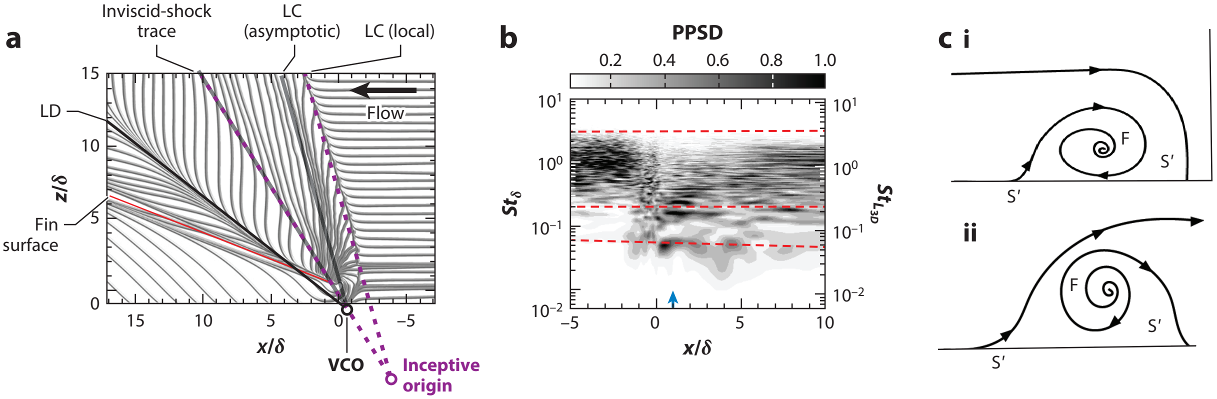

Figure 8

Nonasymptotic effects in regions of inception and symmetry planes. (*a*) Surface-flow lines for the SF SBLI. Lines emanating from the VCO (*black*) best align the surface-flow symmetry in the interior of the interaction. However, lines emanating from the inceptive conical origin (*purple*) best align inceptive features, such as the LC near the shock generator, with the inviscid shock. The red line indicates the infinitesimally thin fin surface. Panel *a* based on Adler & Gaitonde (2020), with permission. (*b*) Premultiplied wall-pressure power spectral density (PPSD) for the SF SBLI as a function of streamwise distance, offset from the fin surface by 0.5δ. The blue arrow indicates the separation location. A prominent peak in the spectra at $St_L \sim 0.05$ occurs beneath the shock in the inceptive region near the fin leading edge; this is reminiscent of 2D scaling. The red lines band the high-frequency range and trace the peak of the low-frequency range. (*c*) Illustration of the complementary patterns of mean-flow streamlines (*i*) in a diverging symmetry plane, such as in front of an obstacle on a plate, and (*ii*) in a converging symmetry plane, such as in the double-fin SBLI. Abbreviations: F, focus; LC, line of coalescence; LD, line of convergence; S′, surface saddle point; SBLI, shock-wave/boundary-layer interactions; SF, sharp fin; *St*, Strouhal number; VCO, virtual conical origin.

the leading edges of shock generators. These edges are necessarily blunted to some degree in practice, resembling the BF in this respect, and a locally curved bow shock arises in this region. Even sharp leading edges incur viscous/inviscid interactions that influence the rapid growth of the boundary layer and, consequently, the local shock shape. It is beneficial for purposes of description to augment the VCO, which is relevant to the asymptotic conical behavior, with an inceptive origin (Adler & Gaitonde 2019) that accounts for deviations near the shock generator and provides a more quantitatively precise measure of inceptive effects. All of these effects diminish with increasing radial displacement from the VCO as conical behavior is recovered.

The size of the region where the interaction deviates from the conical regime (L_{inc}) depends on the flow parameters and increases with the Mach number normal to the shock (M_{n}) and the boundary-layer thickness (δ) as $L_{\mathrm{inc}} \propto M_{\mathrm{n}}\delta^{2/3}$ (Settles & Lu 1985). The boundary-layer thickness can become very large for flight conditions and even for large-scale ground tests; thus, inceptive behavior may dictate the performance more so than asymptotic behavior in these settings. This relates to the conjecture that cylindrical-scaling observations in swept SBLI may be the result of measurements made in inceptive regions due to facility limitations (Settles & Lu 1985, Vanstone et al. 2018).

A method to obtain the inceptive origin is based on the form of the LC; **Figure 8*a*** shows the result for the strongest SF case of Adler & Gaitonde (2020). Quantitative inceptive determinations based on PIV measurements (Vanstone et al. 2018) indicate that the radial distance required to reach conical symmetry depends on the variable chosen for examination. Velocity components of smaller magnitude required longer relaxation lengths than might be estimated from the surface-flow patterns. The relatively higher speed flow outside the separation zone and the corresponding imposed pressure achieve conical similarity more rapidly than the streamwise and crossflow velocities inside the separation zone. Both viscous and turbulent effects, as measured by the Reynolds stresses, also relax more slowly (Adler & Gaitonde 2019).

For several reasons, the distinctions between the experiments and the corresponding, high-fidelity numerical simulations become more important in inceptive regions. Simulations often consider sharp shock-generator leading edges and omit sidewalls and fences, both of which affect the inceptive-region size, that may be present in the experiments. A related issue concerns the possibly stronger dependence on Reynolds number in inceptive regions. For 2D SBLI, and conically asymptotic regions of 3D SBLI, high-fidelity simulations, at notably lower Reynolds numbers than in corresponding experiments, have proven capable of reproducing the main dynamics of interest. This favorable circumstance may not hold in inceptive regions because the rate of growth of the boundary layer on the shock generator and, hence, the leading-edge shock shape depend on Reynolds number. A complete characterization of the Reynolds-number dependence of inceptive effects remains to be achieved.

The region near the leading edge of the shock generator may, in some sense, be considered as a locally 2D (cylindrical) interaction; particularly for weak interactions (small sweep angle), 3D interactions may appear to be cylindrically symmetric at small r. The symmetry plane upstream of a blunted shock generator, topologically represented by the BF configuration, highlights some important considerations; results from this region have been profitably employed, as discussed by Clemens & Narayanaswamy (2014), to examine similarities in unsteadiness between 3D and 2D (cylindrical) SBLI.

This potential connection between the inceptive region and cylindrical behavior bears further scrutiny. The spectral data presented in **Figure 6** were based on a numerical model with a sharp leading edge that does not reproduce the effect of fin bluntness; however, the effects of boundary-layer growth on the fin surface are included, even if imperfectly. A comparison between the experiments and simulations of the spectral content very near the shock generator provides clues as to the dynamic behavior of the inceptive region. **Figure 8*b*** displays the premultiplied wall-pressure PSD very near the leading edge of the fin ($z/\delta = 0.5$), within the inception zone. Because conical symmetry is not anticipated in this zone, the results are plotted as a function of streamwise coordinate (x) rather than azimuthal angle (θ). Relative to the spectra from the asymptotic regions, a more prominent peak of low-frequency content is evident beneath the separation shock ($x/\delta \sim 0$). The frequency of this peak ($St_{L_{3\mathrm{D}}} \sim 0.05$) based on the Strouhal number associated with the local separation length is quite low relative to that in asymptotic regions and is somewhat comparable to the lowest frequency in 2D interactions on the scale of St_L. However, because the separation of scales between the boundary-layer thickness and the local separation length is insignificant in this example, the connection between mechanisms can only be speculated; the clear identification of bands of unsteadiness, as in the pattern of the 2D interactions (**Figure 3**), remains elusive, and correspondences between a frequency range and a mechanism may be misleading if the configuration is materially different.

Indeed, any presumed equivalence between such symmetry planes in truly 3D flows with the equivalent 2D interactions must be evaluated with care, because they are topologically dissimilar (Dallmann 1988). For example, although $\partial u/\partial z$, $\partial v/\partial z$, and w are zero in the mean sense for 3D symmetry planes, $\partial w/\partial z$ is nonzero, and the 3D relief effect associated with the spanwise weakening of the shock wave is absent in 2D SBLI. A possible streamline pattern on the symmetry plane of a 3D flow upstream of an obstacle is sketched in **Figure 8*c*,*i***; comparison with the 2D analog of **Figure 2*b*** shows that the (2D) center is now replaced by a (3D) stable (spiraling inward) focus, which constitutes the trace of the expected necklace or horseshoe vortex. Fluid in the plane first approaches the focus and then leaves the symmetry plane from both sides (diverging). In contrast to the case for 2D SBLI, the 3D separation streamline does not reattach, even in the plane of symmetry.

Higher bifurcations are also possible within this construct, just as with 2D SBLI, in which multiple separation regions may form. For example, the symmetry plane for the CaP exhibits spanwise relief similar to that of the BF/CoP; for the parameters employed by Zuo et al. (2019), a pattern with multiple foci is obtained. The symmetry plane of the DF SBLI (**Figure 8*c*,*ii***) experiences the opposite of a relief effect as flow approaches the symmetry plane from both sides (converging); this pattern has been discussed extensively in the literature (Schmisseur & Gaitonde 2001). Here also, the separating boundary layer does not reattach; rather, the region underneath is occupied by fluid entering the plane through the unstable (spiraling outward) focus. The surface-flow streamlines near such symmetry planes are also pertinent to the discussion of 3D SBLI but are not reviewed here.

The DF SBLI, which is of increasing interest in hypersonic applications, may be viewed as a compound interaction, resulting from the merger of the two quasi-conical interactions, each generated by one of the opposing fins. Recent efforts (Adler & Gaitonde 2022, Seckin et al. 2022) have contributed newer techniques to the classical literature (Zheltovodov 2006, Gaitonde 2015). In this interaction, the behavior near each fin exhibits quasi-conical properties, but new features, including a pair of streamwise-oriented vortices, arise in the central interaction region (Schmisseur & Gaitonde 2001). A particularly interesting aspect of the dynamics is the appearance of a band of lower-frequency unsteadiness that is reminiscent of the separation of frequency scales found in 2D SBLI, while not necessarily reflective of the same underlying mechanisms; this is discussed in detail by Adler & Gaitonde (2022). For these interactions, the dependence of nonasymptotic behavior on Mach and Reynolds numbers has not been adequately characterized; these parameters may strongly affect the scaling considerations between ground and flight tests, as well as correspondences between the former and high-fidelity simulations that tend to consider lower Reynolds numbers for computational feasibility.

Although the CoP (Lindörfer et al. 2020) and CaP (Zuo et al. 2019) interactions display trivial asymptotic behavior, they present unique insights relevant to asymptotically conical interactions. The CaP presents an interesting circumstance because it represents a possible 3D extension of the 2D impinging-shock configuration that includes relief; specifically, in this case, a 3D impinging shock of variable strength (due to curvature) impinges on the boundary layer. The results display neither cylindrical nor conical symmetry; rather, a very intricate, 3D flow structure is observed, with regions of regular and irregular shock reflections from the plate. On the symmetry plane, some topological features are common with the BF/CoP, including the above-noted horseshoe vortex and the associated spanwise pressure gradients; however, the behavior of the boundary layer on the symmetry plane is different because there is no obstacle on the plate for the CaP. Here, 2D relationships, such as those based on the Clauser parameter, remain of interest because of their simplicity, as discussed by Zuo et al. (2019).

4. EMERGENT AND FUTURE WORK IN 3D SBLI

4.1. Complex 3D SBLI and Scaling

This review highlights some recently obtained insights into the significant changes in dynamics that arise when sweep is introduced into 2D SBLI. The connection between the considerably more complicated mean-flow structure and the development of a more prominent convective component to unsteady behavior has become clearer due to the deployment of ever-more-advanced techniques in experiment, simulation, and theory. An immediate need from a long-term application-driven perspective is the continued logical progression toward more intricate SBLI of interest in practical applications: to build on the incomplete knowledge of the DF and triple-shock configurations (Garrison et al. 1996), which introduce new types of compounded behavior in ways that depend more integrally on configuration size and additional geometric parameters. Efforts to develop scaling laws extrapolating from ground to flight tests are especially opportune.

Stability studies that have provided substantial enlightenment in 2D SBLI (for example, Nichols et al. 2017) could prove very rewarding in further deconstructing the unsteady environment of 3D SBLI. These efforts—which could consider classical and more recent approaches, such as resolvent analysis that is capable of nonmodal assessments—are quite difficult to perform in 3D because of the daunting computational expense. Nonetheless, the application of these methods to an isolated region where asymptotic behavior holds may be economical and insightful. A specific construct is the skewed shear layer that forms after separation. The observation that classical free-shear-layer theories apply to 2D SBLI despite the complex, turbulent, near-wall environment is promising, suggesting future directions analogous to those that have provided knowledge on low-speed, 3D, boundary layers (Lozano-Durán et al. 2020). The mean 2D/3C flow (Larsson et al. 2022) or even linear stability analyses of profiles at different points within the interaction may also provide a useful starting point.

4.2. Moving-Shock/Boundary-Layer Interactions

The recent increased interest in high-speed propulsion has highlighted the need to better understand the complex phenomena that occur in inlets and isolators, particularly under conditions in which large-scale shock motion and associated boundary-layer interactions occur. The primary episodes of interest are unstart and mode transition. During unstart, the shock train, which is normally stationary and well established in the duct, propagates upstream, undergoing multiple sequential interactions with the boundary layer and often leading to potentially catastrophic consequences. The associated phenomena are intimately connected to 3D separation, which is typically a key initiator that is susceptible to perturbations from different triggering sources. During mode transition, in contrast, the shock system, initially in a ramjet mode, moves downstream and adopts the state expected for scramjet operation.

The flow in 3D corners is a major consideration; thus, this problem is related to that of confinement, which has been examined extensively to identify the effect of tunnel sidewalls and corners on measurements of presumptively 2D SBLI (Bermejo-Moreno et al. 2014, Xiang & Babinsky 2019). Confinement effects may be characterized as relatively well understood at this time; the typical configuration is a 2D impinging or corner SBLI generator, but with sidewalls. Recent results have greatly enriched the understanding of the complicated, 3D, separated flow in the corner, including manifestations of vortical structures that arise on either side of the symmetry plane (Eagle & Driscoll 2014), regular/irregular transitions in turbulent experiments (Grossman & Bruce 2018), and the significant effect of the length of the shock generator, which was recently explored in laminar computations (Lusher & Sandham 2020). Indeed, a connection may be drawn on some of these aspects to sidewall interactions in classical, asymmetric DF flows (Gaitonde 2015), which have analogous dynamics when rotated by 90° about the streamwise axis.

Recent examination of unsteadiness in sidewall interactions has revealed many features that expand the understanding of the nonasymptotic regions of 3D SBLI discussed in Section 3.3. For example, the simulations of Deshpande & Poggie (2021) indicate that the separated regions near the sidewalls on either side of the symmetry plane retain the signature of unsteadiness of the nominally 2D SBLI that is expected in the center of the channel; the motions of the 3D sidewall regions are correlated in that they display alternating breathing motion, suggesting a particular type of coupling between the main SBLI and the corner flows. Because the initiation and evolution details of unstart are greatly affected by sidewall and corner interactions, these dynamics should be further explored to obtain a better fundamental understanding that translates to the application-driven needs of unstart prediction and avoidance. However, moving-shock/boundary-layer interactions are fundamentally nonstationary; therefore, the typical techniques employed to analyze SBLI dynamics must be supplemented to extract the desired knowledge and generate reduced-order models (ROMs).

4.3. Fluid/Structure Interactions

The amplification of lower frequencies in SBLI relative to those in the undisturbed, upstream turbulent boundary layer can foster coupled structural responses in compliant panels. A further complication arises from thermal considerations because SBLI induce significant localized heating and large wall-temperature gradients. The consequences of aeroelasticity and aerothermoelasticity, including high-cycle material fatigue, vibrations, and failure, can be severe (Dowell 1975, McNamara & Friedmann 2011). The multidisciplinary nature of this problem, the introduction of a much wider range of spatiotemporal scales of interest, and the added sensitivity to initial and boundary conditions amplify the challenges faced by experimental campaigns (Riley et al. 2019, Spottswood et al. 2021) and modeling efforts (Dowell & Hall 2001). Consequently, much remains unknown regarding the conditions required to initiate coupling and the level of fidelity appropriate for analysis. This is true even for FSI arising in 2D SBLI, which trigger 3D responses in size-constrained panels. Significant, recent, nominally 2D SBLI/FSI experiments (Spottswood et al. 2019, Tan et al. 2019) and computations (Shinde et al. 2019, Boyer et al. 2021) provide some insights, but the relevance of the results is limited mostly to the specific configurations examined.

FSI accompanying the swept SBLI of focus here, which are relevant to hypersonic vehicles as discussed by Zuchowski (2012), have been given little attention to date. Even though the Strouhal numbers observed in swept SBLI tend to be higher than in 2D SBLI, coherent structures grow with radial distance, and the frequency reduces (Adler & Gaitonde 2020). Because full-size vehicles exhibit much larger length scales, overlapping flow and panel frequencies will result, and fluid/structure coupling will remain relevant. Swept SBLI introduce additional FSI complications and must consider an even wider range of panel orientations and placements, in both asymptotic and inceptive regions that impose different flow scales.

Although 2D SBLI/FSI results may be of limited direct value in extrapolation to 3D, these campaigns provide guidance to the formulation of a systematic strategy for analyzing FSI associated with swept SBLI. In particular, a stepping-stone study that considers one-way influence of the fluid on the structure, and vice versa, in a loosely coupled setting, may constitute a starting point for more advanced, fully coupled analyses that leverage, to the extent possible, ROMs and other simplifying choices. Some possibilities are listed below with citations to analogous procedures for 2D SBLI, but with the understanding that the parameter range would include the consideration of panels with different sizes and orientations relative to the conical or inceptive features of the swept SBLI, along with an extended parameter range due to the more complex geometric dependence of the flow scales. The use of piston theory offers a relatively simple approach for initial studies (Meijer & Dala 2016). A more accurate knowledge of surface-pressure fluctuations in swept SBLI without FSI, obtained, for example, with pressure-sensitive paint (Mears et al. 2020) or high-fidelity simulations (Adler & Gaitonde 2020), could offer a higher level of insight, especially if combined with model-reduction frameworks (Dowell & Hall 2001, Crowell & McNamara 2012). At the next level, the response of the flow to prescribed static and dynamic deformation (one-way coupling) may be considered; a recent example of this is the work of Brouwer et al. (2017), who successfully used RANS to examine the effect of compliance on 2D-SBLI-induced separation.

Indeed, the known inviscid/rotational structure of swept SBLI (Knight et al. 1987) may facilitate affordable, 3D, viscous and inviscid analyses, such as those by Visbal (2014) for aeroelastic flutter.

The smaller spatiotemporal scales in the ground-test environment and the reduced Reynolds numbers associated with high-fidelity simulations introduce difficulties in establishing the dynamic similitude required to elicit a coupled response. Innovative leveraging of nondimensionalization techniques and dynamic similarity considerations (Dugundji & Calligeros 1962) may help guide the formulation of a suitably circumscribed test matrix. Surrogate materials chosen to trigger a desirable response, rather than for actual use, are a possible solution (Pham et al. 2018). Some recent efforts have introduced oscillating shocks of controlled frequencies to provide impinging-shock SBLI loads on compliant panels; recent experiments in this vein are reported by Daub et al. (2015), Neet & Austin (2020), and Vasconcelos et al. (2022), along with high-fidelity simulations by Pasquariello et al. (2015). An analogous campaign for swept SBLI could oscillate the fin (for example), which may require innovative configuration design. The transient, possibly decaying response of an initially deformed panel in the presence of a swept SBLI flow could also facilitate an intermediate understanding, short of the fully coupled interaction. The collective information obtained from carefully selected problems that isolated different aspects of the complex FSI could then be used to formulate a fully coupled, grand challenge problem that ensured robust, compliant, panel response, similar to that anticipated in flight, through an integrated experimental/computational campaign.

SBLI-induced aerothermoelastic analyses are predicated on additional considerations that bring in conjugate heat-transfer considerations due to wall-temperature gradients and heat-transfer rates; Dolling (2001) highlighted associated difficulties regarding the measurement and simulation of these phenomena, even without FSI. Recent work in 2D transitional and turbulent SBLI over a wide range of Mach numbers, without (Sandham et al. 2014, Bernardini et al. 2016, Fu et al. 2021) and with (Whalen et al. 2020) FSI, again provides a pathway for 3D-SBLI studies, although the corresponding effort required is daunting.

4.4. Flow Control

Several objectives may be postulated for SBLI control. Perhaps the most common goal to date has been the reduction of flow separation and distortion prior to combustion for better aircraft engine performance. Bleed has been a traditionally popular method (see, for example, Harloff & Smith 1996); however, because bleed incurs penalties in the form of increased drag, weight, and (for internal flows) some reduction of propulsive mass flow rate, recent efforts utilizing passive techniques have focused on bumps and vortex generators (VGs). These efforts have also extended the objectives to include the reduction of unsteadiness. Bruce & Colliss (2015) discussed the mechanisms by which bumps reduce or eliminate separation in transitional and turbulent 2D SBLI. Methods to derive optimal bump characteristics have been developed; for example, structurally feasible morphing may be employed with local separation-based sensing (Shinde et al. 2020), and a successful implementation of the method in a complex flowpath has been tested experimentally (Schülein et al. 2022). Other noteworthy passive-control efforts involve establishing recirculation (downstream suction and upstream blowing) employing the pressure differential upstream and downstream of the shock (Pasquariello et al. 2014), microramps (Schreyer et al. 2021), and compliant surfaces (Visbal 2014, Pham et al. 2018, Gomez-Vega et al. 2020), the last of which also facilitate the examination of SBLI/FSI.

There have been relatively fewer investigations of 3D-SBLI control; however, some recent appraisals provide a guide for future activity. Both passive and active efforts to date appear to require that the actuator be placed relatively close to the interaction for effectiveness; results using

VGs on a fin-on-cylinder, swept SBLI demonstrate this effectively (Pickles & Narayanaswamy 2020). This approach may introduce immense challenges when flow conditions change at off-design conditions. The localized effect of protuberances was also measured by Padmanabhan et al. (2020) when exploring the edge effects of swept impinging-shock SBLI. Active-control methods have similarly revealed the importance of actuator placement location. For example, microjets (blowing) display better control authority if placed in the inceptive region, as in Mears et al. (2021), who note that the actuator mass flow rate is the primary determinant of control authority; altering the frequency of actuation did not provide any notable advantage. These results are consistent with prior 2D-SBLI efforts of Webb et al. (2013), who saw only modest effects with high-bandwidth plasma-based actuators.

In general, there is a clear need for new innovative approaches to SBLI control, including for the more complex 3D interactions. Exploiting the benefits of active control will require a better understanding of the sensitivity of swept SBLI to small perturbations; such understanding has aided the design of effective control strategies in lower-ranked systems. The region near the fin leading edge (the inceptive region) may be the best location for maximizing the global influence of the control method, because the observed coherent structures sweep in the spanwise direction. The stability and resolvent-type analyses suggested in Section 4.1 may serve a very useful purpose in this context; they could be employed to identify optimal actuator placement and properties (mass, momentum, energy, or relevant combinations), in which a minimal input could provide the maximum effect. Control strategies that leverage small perturbations to achieve control goals are the most likely to prove scalable to larger systems.

5. CONCLUSION

The breakdown of spanwise homogeneity in (2D) shock-wave/boundary-layer interactions can occur in many different ways, resulting in a multitude of possible 3D interactions; a clearer understanding of the principles that underlie the dynamics of these 3D SBLI is required. Recent efforts that have focused on unique aspects of these interactions, substantially adding to the body of classical literature, are reviewed above. Although a very diverse set of geometric configurations for 3D interactions are of interest from an application-driven perspective, a necessary degree of unification of description is facilitated by considering interactions with conically asymptotic behavior, namely swept, semi-infinite interactions; configuration-dependent deviations from asymptotic behavior may then be included to complete each description. For strongly swept, asymptotic interactions, recent efforts, leveraging new diagnostics and simulation capabilities, have identified key distinctions of their dynamic properties relative to analogous 2D interactions. The lower-frequency unsteadiness of conical interactions exhibits a relatively more significant convective character that is associated with phenomena of separated shear layers, whereas the unsteadiness associated with interaction breathing is relatively muted. These observations are related to differences in the properties of the mean flow, in which conical interactions exhibit a spatially dependent mixture of 2D and 3D shear-layer length scales, which are reflected in the resulting frequency content. The stability properties of 2D SBLI have recently been further clarified, providing a framework for analogous analyses of 3D SBLI; the comparatively more convective nature of 3D SBLI is also manifest in the character of the dominant instability. The change in dynamic behavior near a shock generator, within inceptive regions, or in the vicinity of symmetry planes is also instructive; however, care must be exercised when associating 2D character with such regions. This review leverages these and other recent observations to identify several potentially consequential next steps in 3D-SBLI research that combine fundamental aspects with increasingly imperative practical motivations.

DISCLOSURE STATEMENT

The authors are not aware of any biases that might be perceived as affecting the objectivity of this review.

ACKNOWLEDGMENTS

The authors express gratitude to a number of colleagues for extended discussions on SBLI, including L. Agostini, F. Alvi, N. Bisek, N. Clemens, J.-P. Dussauge, J. McNamara, J. Poggie, J. Schmisseur, V. Shinde, M. Spottswood, L. Vanstone, and M. Visbal. The help of students N. Arora, S. Baugher, P. Doshi, and J. Thayer is also acknowledged. The authors' work was performed under various prior grants from the Air Force Office of Scientific Research and computational resources from the Department of Defense High Performance Computing Modernization Program, which are gratefully acknowledged. Lawrence Livermore National Laboratory is operated by Lawrence Livermore National Security, LLC, for the US Department of Energy, National Nuclear Security Administration, under contract DE-AC52-07NA27344.

LITERATURE CITED

Adler MC, Gaitonde DV. 2018. Dynamic linear response of a shock/turbulent-boundary-layer interaction using constrained perturbations. *J. Fluid Mech.* 840:291–341

Adler MC, Gaitonde DV. 2019. Flow similarity in strong swept-shock/turbulent-boundary-layer interactions. *AIAA J.* 57(4):1579–93

Adler MC, Gaitonde DV. 2020. Dynamics of strong swept-shock/turbulent-boundary-layer interactions. *J. Fluid Mech.* 896:A29

Adler MC, Gaitonde DV. 2022. Influence of separation structure on the dynamics of shock/turbulent-boundary-layer interactions. *Theor. Comput. Fluid Dyn.* 36:303–26

Agostini L, Larchevêque L, Dupont P, Debiève JF, Dussauge JP. 2012. Zones of influence and shock motion in a shock/boundary-layer interaction. *AIAA J.* 50(6):1377–87

Andreopoulos J, Muck KC. 1987. Some new aspects of the shock-wave/boundary-layer interaction in compression-ramp flows. *J. Fluid Mech.* 180:405–28

Andreopoulos Y, Agui JH, Briassulis G. 2000. Shock wave–turbulence interactions. *Annu. Rev. Fluid Mech.* 32:309–45

Arora N, Ali MY, Zhang Y, Alvi FS. 2018. Flowfield measurements in a Mach 2 fin-generated shock/boundary-layer interaction. *AIAA J.* 56(10):3963–74

Arora N, Mears L, Alvi FS. 2019. Unsteady characteristics of a swept-shock/boundary-layer interaction at Mach 2. *AIAA J.* 57(10):4548–59

Aubard G, Gloerfelt X, Robinet JC. 2013. Large-eddy simulation of broadband unsteadiness in a shock/boundary-layer interaction. *AIAA J.* 51(10):2395–409

Bae HJ, Dawson STM, McKeon BJ. 2020. Resolvent-based study of compressibility effects on supersonic turbulent boundary layers. *J. Fluid Mech.* 883:A29

Baldwin A, Mears LJ, Arora N, Kumar R, Alvi FS, Naughton JW. 2019. Skin friction measurements using oil film interferometry in a 3-D supersonic flowfield. *AIAA J.* 57(4):1373–82

Baldwin A, Mears LJ, Kumar R, Alvi FS. 2021. Effects of Reynolds number on swept shock-wave/boundary-layer interactions. *AIAA J.* 59(10):3883–99

Beneddine S, Sipp D, Arnault A, Dandois J, Lesshafft L. 2016. Conditions for validity of mean flow stability analysis. *J. Fluid Mech.* 798:485–504

Bermejo-Moreno I, Campo L, Larsson J, Bodart J, Helmer D, Eaton JK. 2014. Confinement effects in shock wave/turbulent boundary layer interactions through wall-modelled large-eddy simulations. *J. Fluid Mech.* 758:5–62

Bernardini M, Asproulias I, Larsson J, Pirozzoli S, Grasso F. 2016. Heat transfer and wall temperature effects in shock wave turbulent boundary layer interactions. *Phys. Rev. Fluids* 1(8):084403

Boyer NR, McNamara J, Gaitonde D, Barnes CJ, Visbal MR. 2021. Features of panel flutter response to shock boundary layer interactions. *J. Fluids Struct.* 101:103207

Brouwer KR, Gogulapati A, McNamara JJ. 2017. Interplay of surface deformation and shock-induced separation in shock/boundary-layer interactions. *AIAA J.* 55(12):4258–73

Brown GL, Roshko A. 1974. On density effects and large structure in turbulent mixing layers. *J. Fluid Mech.* 64(4):775–816

Bruce P, Colliss S. 2015. Review of research into shock control bumps. *Shock Waves* 25(5):451–71

Chapman D, Kuehn D, Larson H. 1957. *Investigation of separated flows in supersonic and subsonic streams with emphasis on the effect of transition*. NACA-TR-1356, Ames Aeronaut. Lab., Moffett Field, Calif.

Clemens NT, Narayanaswamy V. 2014. Low-frequency unsteadiness of shock wave/turbulent boundary layer interactions. *Annu. Rev. Fluid Mech.* 46:469–92

Crowell AR, McNamara JJ. 2012. Model reduction of computational aerothermodynamics for hypersonic aerothermoelasticity. *AIAA J.* 50(1):74–84

Dallmann U. 1988. Three-dimensional vortex structures and vorticity topology. *Fluid Dyn. Res. Jpn. Soc. Fluid Mech.* 3(1–4):183–89

Daub D, Willems S, Gülhan A. 2015. Experiments on the interaction of a fast-moving shock with an elastic panel. *AIAA J.* 54(2):670–78

Délery JM. 2001. Robert Legendre and Henri Werlé: toward the elucidation of three-dimensional separation. *Annu. Rev. Fluid Mech.* 33:129–54

Deshpande AS, Poggie J. 2021. Large-scale unsteadiness in a compression ramp flow confined by sidewalls. *Phys. Rev. Fluids* 6(2):024610

Di Renzo M, Oberoi N, Larsson J, Pirozzoli S. 2022. Crossflow effects on shock wave/turbulent boundary layer interactions. *Theor. Comput. Fluid Dyn.* 36:327–44

Doehrmann AC, Threadgill JAS, Little JC. 2018. *Effect of sweep on the mean and unsteady structures of impinging shock/boundary layer interactions*. Presented at AIAA Aerosp. Sci. Meet., Kissimmee, Fla., AIAA Pap. 2018-2074, Jan. 8–12

Dolling DS. 2001. Fifty years of shock-wave/boundary-layer interaction research: what next? *AIAA J.* 39(8):1517–31

Dowell EH. 1975. *Aeroelasticity of Plates and Shells*. Leyden, Neth.: Noordhoff Int.

Dowell EH, Hall KC. 2001. Modeling of fluid-structure interaction. *Annu. Rev. Fluid Mech.* 33:445–90

Dugundji J, Calligeros JM. 1962. Similarity laws for aerothermoelastic testing. *J. Aerosp. Sci.* 29(8):935–50

Dupont P, Haddad C, Debiève J. 2006. Space and time organization in a shock-induced separated boundary layer. *J. Fluid Mech.* 559:255–77

Dupont P, Piponniau S, Dussauge JP. 2019. Compressible mixing layer in shock-induced separation. *J. Fluid Mech.* 863:620–43

Dwivedi A, Hildebrand N, Nichols JW, Candler GV, Jovanović MR. 2020. Transient growth analysis of oblique shock-wave/boundary-layer interactions at Mach 5.92. *Phys. Rev. Fluids* 5(6):063904

Eagle WE, Driscoll JF. 2014. Shock wave–boundary layer interactions in rectangular inlets: three-dimensional separation topology and critical points. *J. Fluid Mech.* 756:328–53

Erengil M, Dolling D. 1993. Effects of sweepback on unsteady separation in Mach 5 compression ramp interactions. *AIAA J.* 31(2):302–11

Estruch-Samper D, Chandola G. 2018. Separated shear layer effect on shock-wave/turbulent-boundary-layer interaction unsteadiness. *J. Fluid Mech.* 848:154–92

Fu L, Karp M, Bose ST, Moin P, Urzay J. 2021. Shock-induced heating and transition to turbulence in a hypersonic boundary layer. *J. Fluid Mech.* 909:A8

Gaitonde DV. 2015. Progress in shockwave/boundary layer interactions. *Prog. Aerosp. Sci.* 72:80–99

Ganapathisubramani B, Clemens N, Dolling D. 2007. Effects of upstream boundary layer on the unsteadiness of shock-induced separation. *J. Fluid Mech.* 585:369–94

Garrison T, Settles G, Horstman C. 1996. Measurements of the triple shock wave/turbulent boundary-layer interaction. *AIAA J.* 34(1):57–64

Gibson BT, Dolling DS. 1992. Exploratory study of wall pressure fluctuations in a Mach 5, sharp fin–induced turbulent interaction. *AIAA J.* 30(9):2188–95

Gomez-Vega N, Gramola M, Bruce PJK. 2020. Oblique shock control with steady flexible panels. *AIAA J.* 58(5):2109–21

Green J. 1970. Interactions between shock waves and turbulent boundary layers. *Prog. Aerosp. Sci.* 11:235–340

Gross A, Little J, Fasel HF. 2022. Numerical investigation of unswept and swept turbulent shock-wave boundary layer interactions. *Aerosp. Sci. Technol.* 123:107455

Grossman IJ, Bruce PJK. 2018. Confinement effects on regular–irregular transition in shock-wave–boundary-layer interactions. *J. Fluid Mech.* 853:171–204

Guiho F, Alizard F, Robinet JC. 2016. Instabilities in oblique shock wave/laminar boundary-layer interactions. *J. Fluid Mech.* 789:1–35

Harloff GJ, Smith GE. 1996. Supersonic-inlet boundary-layer bleed flow. *AIAA J.* 34(4):778–85

Helm CM, Martín MP, Williams OJ. 2021. Characterization of the shear layer in separated shock/turbulent boundary layer interactions. *J. Fluid Mech.* 912:A7

Karban U, Bugeat B, Martini E, Towne A, Cavalieri AVG, et al. 2020. Ambiguity in mean-flow-based linear analysis. *J. Fluid Mech.* 900:R5

Kim K, Lee Y, Alvi F, Settles G, Horstman C. 1991. Skin-friction measurements and computational comparison of swept shock/boundary-layer interactions. *AIAA J.* 29(10):1643–50

Knight DD, Horstman C, Bogdonoff S, Shapey B. 1987. Structure of supersonic turbulent flow past a sharp fin. *AIAA J.* 25(10):1331–37

Korkegi RH. 1975. Comparison of shock-induced two- and three-dimensional incipient turbulent separation. *AIAA J.* 13(4):534–35

Larsson J, Kumar V, Oberoi N, Di Renzo M, Pirozzoli S. 2022. Large-eddy simulations of idealized shock/boundary-layer interactions with crossflow. *AIAA J.* 60(5):2767–70

Lash LE, Gragston M, Kreth PA, McDaniel Z, Coder JG, Schmisseur JD. 2021. Upstream influence in shock wave/transitional boundary layer interactions at Mach 1.8. *AIAA J.* 59(12):4842–57

Lindörfer SA, Combs CS, Kreth PA, Bond RB, Schmisseur JD. 2020. Scaling of cylinder-generated shock-wave/turbulent boundary-layer interactions. *Shock Waves* 30(4):395–407

Lozano-Durán A, Giometto MG, Park GI, Moin P. 2020. Non-equilibrium three-dimensional boundary layers at moderate Reynolds numbers. *J. Fluid Mech.* 883:A20

Lusher DJ, Sandham ND. 2020. The effect of flow confinement on laminar shock-wave/boundary-layer interactions. *J. Fluid Mech.* 897:A18

McNamara JJ, Friedmann PP. 2011. Aeroelastic and aerothermoelastic analysis in hypersonic flow: past, present, and future. *AIAA J.* 49(6):1089–122

Mears LJ, Baldwin A, Ali MY, Kumar R, Alvi FS. 2020. Spatially resolved mean and unsteady surface pressure in swept SBLI using PSP. *Exp. Fluids* 61(4):92

Mears LJ, Sellappan P, Alvi FS. 2021. Three-dimensional flowfield in a fin-generated shock wave/boundary-layer interaction using tomographic PIV. *AIAA J.* 59(12):4869–80

Meijer MC, Dala L. 2016. Generalized formulation and review of piston theory for airfoils. *AIAA J.* 54(1):17–27

Morgan B, Duraisamy K, Nguyen N, Kawai S, Lele S. 2013. Flow physics and RANS modelling of oblique shock/turbulent boundary layer interaction. *J. Fluid Mech.* 729:231–84

Neet MC, Austin JM. 2020. *Effects of surface compliance on shock boundary layer interaction in the Caltech Mach 4 Ludwieg tube*. Presented at AIAA Scitech Forum, Orlando, Fla., AIAA Pap. 2020-0816, Jan. 6–10

Nichols JW, Larsson J, Bernardini M, Pirozzoli S. 2017. Stability and modal analysis of shock/boundary layer interactions. *Theor. Comput. Fluid Dyn.* 31(1):33–50

Padmanabhan S, Castro Maldonado J, Threadgill JA, Little JC. 2020. *Root influence on the unsteady characteristics of swept impinging oblique SBLIs*. Presented at AIAA Scitech Forum, Orlando, Fla., AIAA Pap. 2020-0580, Jan. 6–10

Padmanabhan S, Maldonado JC, Threadgill JAS, Little JC. 2021. Experimental study of swept impinging oblique shock/boundary-layer interactions. *AIAA J.* 59(1):140–49

Panaras AG. 1996. Review of the physics of swept-shock/boundary layer interactions. *Prog. Aerosp. Sci.* 32:173–244

Pasquariello V, Grilli M, Hickel S, Adams NA. 2014. Large-eddy simulation of passive shock-wave/boundary-layer interaction control. *Int. J. Heat Fluid Flow* 49:116–27

Pasquariello V, Hickel S, Adams N, Hammerl G, Wall W, et al. 2015. *Coupled simulation of shock-wave/turbulent boundary-layer interaction over a flexible panel*. Paper presented at the 6th European Conference for Aerospace Sciences, Krakow, Pol., June 29–July 3

Pasquariello V, Hickel S, Adams NA. 2017. Unsteady effects of strong shock-wave/boundary-layer interaction at high Reynolds number. *J. Fluid Mech.* 823:617–57

Perry A, Chong M. 1987. A description of eddying motions and flow patterns using critical-point concepts. *Annu. Rev. Fluid Mech.* 19:125–55

Pham HT, Gianikos ZN, Narayanaswamy V. 2018. Compression ramp induced shock-wave/turbulent boundary-layer interactions on a compliant material. *AIAA J.* 56(7):2925–29

Pickles JD, Narayanaswamy V. 2020. Control of fin shock induced flow separation using vortex generators. *AIAA J.* 58(11):4794–806

Piponniau S, Dussauge JP, Debiève JF, Dupont P. 2009. A simple model for low-frequency unsteadiness in shock-induced separation. *J. Fluid Mech.* 629:87–108

Pirozzoli S, Grasso F. 2006. Direct numerical simulation of impinging shock wave/turbulent boundary layer interaction at $M = 2.25$. *Phys. Fluids* 18(6):065113

Pirozzoli S, Larsson J, Nichols J, Bernardini M, Morgan B, Lele S. 2010. Analysis of unsteady effects in shock/boundary layer interactions. *Annu. Res. Briefs* 2010:153–64

Poggie J, Bisek NJ, Kimmel RL, Stanfield SA. 2014. Spectral characteristics of separation shock unsteadiness. *AIAA J.* 53(1):200–14

Porter KM, Poggie J. 2019. Selective upstream influence on the unsteadiness of a separated turbulent compression ramp flow. *Phys. Fluids* 31(1):016104

Priebe S, Martín MP. 2012. Low-frequency unsteadiness in shock wave–turbulent boundary layer interaction. *J. Fluid Mech.* 699:1–49

Priebe S, Tu JH, Rowley CW, Martín MP. 2016. Low-frequency dynamics in a shock-induced separated flow. *J. Fluid Mech.* 807:441–77

Riley ZB, Perez RA, Bartram GW, Spottswood SM, Smarslok BP, Beberniss TJ. 2019. Aerothermoelastic experimental design for the AEDC/VKF Tunnel C: challenges associated with measuring the response of flexible panels in high-temperature, high-speed wind tunnels. *J. Sound Vib.* 441:96–105

Sandham ND. 2016. Effects of compressibility and shock-wave interactions on turbulent shear flows. *Flow Turbul. Combust.* 97(1):1–25

Sandham ND, Schülein E, Wagner A, Willems S, Steelant J. 2014. Transitional shock-wave/boundary-layer interactions in hypersonic flow. *J. Fluid Mech.* 752:349–82

Sansica A, Sandham N, Hu Z. 2014. Forced response of a laminar shock-induced separation bubble. *Phys. Fluids* 26(9):093601

Saric WS, Reed HL, White EB. 2003. Stability and transition of three-dimensional boundary layers. *Annu. Rev. Fluid Mech.* 35:413–40

Sasaki K, Barros DC, Cavalieri AVG, Larchevêque L. 2021. Causality in the shock wave/turbulent boundary layer interaction. *Phys. Rev. Fluids* 6(6):064609

Schmid PJ, Henningson DS. 2012. *Stability and Transition in Shear Flows* (Applied Mathematical Sciences, Vol. 142). New York: Springer

Schmisseur JD, Dolling DS. 1994. Fluctuating wall pressures near separation in highly swept turbulent interactions. *AIAA J.* 32(6):1151–57

Schmisseur JD, Gaitonde DV. 2001. Numerical investigation of strong crossing shock-wave/turbulent boundary-layer interactions. *AIAA J.* 39(9):1742–49

Schreyer AM, Sahoo D, Williams OJH, Smits AJ. 2021. Influence of a microramp array on a hypersonic shock-wave/turbulent boundary-layer interaction. *AIAA J.* 59(6):1924–39

Schülein E, Schnepf C, Weiss S. 2022. Concave bump for impinging-shock control in supersonic flows. *AIAA J.* 60(5):2749–66

Seckin S, Mears LJ, Song M, Zigunov F, Sellappan P, Alvi FS. 2022. *Surface properties of double-fin generated shock-wave/boundary-layer interactions*. Presented at AIAA Scitech Forum, San Diego, Calif./virtual, AIAA Pap. 2022-0701, Jan. 3–7

Settles GS, Dodson LJ. 1994. Supersonic and hypersonic shock/boundary-layer interaction database. *AIAA J.* 32(7):1377–83

Settles GS, Dolling DS. 1986. Swept shock wave/boundary-layer interactions. In *AIAA Progress in Astronautics and Aeronautics: Tactical Missile Aerodynamics*, Vol. 104, ed. M Hemsch, J Nielsen, pp. 297–379. New York: AIAA

Settles GS, Lu FK. 1985. Conical similarity of shock/boundary-layer interactions generated by swept and unswept fins. *AIAA J.* 23(7):1021–27

Settles GS, Teng HY. 1984. Cylindrical and conical flow regimes of three-dimensional shock/boundary-layer interactions. *AIAA J.* 22(2):194–200

Shinde V, McNamara J, Gaitonde D. 2020. Control of transitional shock wave boundary layer interaction using structurally constrained surface morphing. *Aerosp. Sci. Technol.* 96:105545

Shinde V, McNamara J, Gaitonde D, Barnes C, Visbal M. 2019. Transitional shock wave boundary layer interaction over a flexible panel. *J. Fluids Struct.* 90:263–85

Souverein LJ, Dupont P, Debiève JF, Van Oudheusden BW, Scarano F. 2010. Effect of interaction strength on unsteadiness in shock-wave-induced separations. *AIAA J.* 48(7):1480–93

Spottswood SM, Beberniss TJ, Eason TG, Perez RA, Donbar JM, et al. 2019. Exploring the response of a thin, flexible panel to shock-turbulent boundary-layer interactions. *J. Sound Vib.* 443:74–89

Spottswood SM, Smarslok BP, Perez RA, Beberniss TJ, Hagen BJ, et al. 2021. Supersonic aerothermoelastic experiments of aerospace structures. *AIAA J.* 59(12):5029–48

Tan DKM, Tran TT, Bogdonoff SM. 1987. Wall pressure fluctuations in a three-dimensional shock-wave/turbulent boundary interaction. *AIAA J.* 25(1):14–21

Tan SS, Bruce PJ, Gramola M. 2019. *Oblique shockwave boundary layer interaction on a flexible surface*. Presented at AIAA Scitech Forum, San Diego, Calif., AIAA Pap. 2019-0097, Jan. 7–11

Touber E, Sandham N. 2009. Large-eddy simulation of low-frequency unsteadiness in a turbulent shock-induced separation bubble. *Theor. Comput. Fluid Dyn.* 23:79–107

Unnikrishnan S, Gaitonde DV. 2016. A high-fidelity method to analyze perturbation evolution in turbulent flows. *J. Comput. Phys.* 310:45–62

Vanstone L, Clemens NT. 2019. Proper orthogonal decomposition analysis of swept-ramp shock-wave/boundary-layer unsteadiness at Mach 2. *AIAA J.* 57(8):3395–409

Vanstone L, Goller T, Mears L, Clemens NT. 2019. *Separated flow unsteadiness in a Mach 2 swept compression-ramp interaction using high-speed PSP*. Presented at AIAA Aviat. Forum, Dallas, Tex., AIAA Pap. 2019-3647, June 17–21

Vanstone L, Musta MN, Seckin S, Clemens NT. 2018. Experimental study of the mean structure and quasi-conical scaling of a swept-compression-ramp interaction at Mach 2. *J. Fluid Mech.* 841:1–27

Vasconcelos PB, McQuellin L, Talluru K, Neely A. 2022. *Hypersonic fluid-structure interactions on a compliant clamped-free-clamped-free panel under the influence of static shock impingement*. Presented at AIAA Scitech Forum, San Diego, Calif./virtual, AIAA Pap. 2022-0241, Jan. 3–7

Visbal M. 2014. Viscous and inviscid interactions of an oblique shock with a flexible panel. *J. Fluids Struct.* 48:27–45

Webb N, Clifford C, Samimy M. 2013. Control of oblique shock wave/boundary layer interactions using plasma actuators. *Exp. Fluids* 54(6):1545

Whalen TJ, Schöneich AG, Laurence SJ, Sullivan BT, Bodony DJ, et al. 2020. Hypersonic fluid–structure interactions in compression corner shock-wave/boundary-layer interaction. *AIAA J.* 58(9):4090–105

Xiang X, Babinsky H. 2019. Corner effects for oblique shock wave/turbulent boundary layer interactions in rectangular channels. *J. Fluid Mech.* 862:1060–83

Zheltovodov A. 2006. *Some advances in research of shock wave turbulent boundary layer interactions*. Presented at AIAA Aerosp. Sci. Meet., 44th, Reno, Nev., AIAA Pap. 2006-496, Jan. 9–12

Zuchowski B. 2012. *Predictive capability for hypersonic structural response and life prediction. Phase I. Identification of knowledge gaps*. Tech. Rep. AFRL-RB-WP-TR-2012-0280, Air Force Res. Lab., Wright-Patterson AFB, Ohio

Zuo FY, Memmolo A, Huang GP, Pirozzoli S. 2019. Direct numerical simulation of conical shock wave–turbulent boundary layer interaction. *J. Fluid Mech.* 877:167–95

Annual Review of Fluid Mechanics

Volume 55, 2023

Contents

Indexes

Errata

An online log of corrections to *Annual Review of Fluid Mechanics* articles may be found at http://www.annualreviews.org/errata/fluid